UNIVERSITÄT OSNABRÜCK

Structural and electronic study of Silicon doped structures: Aggregates, Wires, and Bulk Systems

DISSERTATION

submitted for the degree of
Dr. rer. nat. (Doctor rerum naturalium)
in the Department of Physics
University of Osnabrück, Germany
by

Homero Cantera-López

October 2011

Acknowledgements

This work was supported by the Deutsche Forschungsgemeinschaft (Graduate College 695).

Contents

List of Figures

List of Tables

1

Introduction

Possible technical applications of Si nanoclusters, both pure [1] and doped with transition metal atoms [2], have originated many studies and raised interesting questions about their electronic and structural properties.

Pure Si_n clusters, as inferred from experimental measurements [3–6], are prolate for $n < 27$ and become nearly spherical for $n > 27$, which has been corroborated by computational studies [1, 7–16]. On the other hand, the growth behavior of transition-metal (M) doped silicon clusters seems to follow a different pattern than pure Si clusters. There are several calculations of MSi_n structures for various cluster sizes and impurity atoms or ions. Kumar and co-workers [16, 17] have found that open basket like structures are the most favorable for $n = 8 - 12$, while for $n = 13 - 16$ the metal atom is completely surrounded by Si atoms. The optimal cage for many of the metal-encapsulated silicon clusters occurs at $n = 16$ [2, 18]. These predictions were later confirmed indirectly by experiments. Experiments on photodissociation of MSi_n [19] clusters indicate that, for M=Cr, encapsulation of Cr occurs at $n = 15$ and 16. A mass spectrometric stability study of binary MS_n clusters [20] with S=Si, Ge, Sn, Pb, and M=Cr, Mn, Cu, Zn, reveals interesting trends. For example, Cr-doped silicon cationic clusters are peculiarly abundant at sizes n=15 and 16, as already obtained by Beck twenty years ago [21, 22]. Other experiments, combining mass spectrometry, a chemical probe method, and photoelectron spectroscopy [23], revealed that one metal atom (M=Ti, Hf, Mo, W) can be encapsulated inside a Si_n cage at $n = 15$. In recent mass spectrometry experiments, Nakajima and co-workers [24] have shown the size-selective formation of $Si_{16}Sc^-$, $Si_{16}Ti$, and $Si_{16}V^+$ clusters. More details about these experiments, combining mass spectrometry, anion photoelectron spectroscopy, and adsorption reactivity towards H_2O, have been published very recently [25].

Concerning the special stability of $Si_{16}M$ for the type of M impurity involved in the experiments of Nakajima and co-workers, we have found only very few publications. Kumar and Kawazoe [18] obtained for $Si_{16}Ti$ a truncated tetrahedral structure, called the Frank-Kasper (FK) polyhedron. In further work Kumar and co-workers explained the special stability of that cluster in terms of a spherical potential model [26–28], as a combination of geometrical and electronic shell effects. In the work of Reveles and Khana [29], cationic, neutral, and anionic doped clusters MSi_n with $n = 15 - 17$, were optimized. These authors obtained that $Si_{16}M$ clusters with $M{=}Sc^-$, Ti, V^+, adopt the FK-polyhedron structure in their ground state, having the highest occupied molecular orbital-lowest unoccupied molecular orbital (HOMO-LUMO) gap and the atomization energy larger than the same clusters in other charge states, which is a manifestation of stability against changes in the electronic charge. The explanation of this fact was based on a 20 electron rule, assuming that only one electron is contributed by a Si atom to the valence manifold when that Si atom is bonded to the metal atom.

The present work focuses on the electronic and structural properties of Ta-Si-F aggregates. We study positively charged $Ta^+@Si_n$ clusters, neutral $Ta@Si_{16}F$ clusters, and aggregates built from $Ta@Si_{16}F$ units. This covers also bulk phases and one-dimensional infinite wires. We discover that an aggregate built by arranging vertically two triangular $Ta@Si_{16}F$ trimers shows special stability and contains a central cavity large enough to encapsulate small molecules. An infinite wire constructed from that aggregate is also studied. The last issue of the present work is the problem of encapsulation of small molecules like H_2 and H_2O into such aggregates and wires.

The organization of this thesis is the following:

In Chapter 2 we describe the basic theoretical aspects of our calculation method. This text can be found in the textbook of Leach [30] and Söderlind [31], and in the review article of Schwarz and Blaha [32].

In Chapter 3 we explain the calculation tools used in this work namely, the SIESTA (Spanish Initiative for Electronic Simulations with Thousands of Atoms) code basic capabilities and some of the core theoretical background of that code. In this Chapter we also explain the most important computational details used in our calculations, like the atomic electronic configurations, basis sets, and some precision parameters.

In Chapters 4–8 we present our main results and discuss them. We begin with the study of $Ta^{+}@Si_{n=14-18}$ cations, the next Chapters are dedicated to the study of $Ta@Si_{16}F$: cluster, aggregates, bulk, and wires.

The last results, presented in Chapter 8, are those of the adsorption of small molecules into the $Ta@Si_{16}F$ superatom and the $(Ta@Si_{16}F)_6$ aggregate and wire.

Finally, in Chapter 9 we present a summary of the results of the present work.

2

Density Functional Theory and methodology

Introduction

The theoretical possibility to study complex crystalline systems containing many atoms is to perform computer simulations. This can be performed with a variety of methods ranging from classical to quantum mechanical (QM) approaches. The former are force field or semi-empirical schemes, in which the forces that determine the interactions between the atoms are parameterized in order to reproduce a series of experimental data, such as equilibrium geometries, bulk modulus or lattice vibrational frequencies (phonons). These schemes have reached a high level of sophistication and are often useful within a given class of materials provided good parameters are already known. If, however, such parameters are not available, or if a system shows unusual phenomena that are not yet understood, one must rely only on *ab initio* calculations. They are more demanding in terms of computer requirements and thus allow only the treatment of much smaller unit cells than semi-empirical calculations do. The advantage of first-principle methods lies in the fact that they do not require any experimental knowledge to carry out such calculations. The following presentation will be restricted to *ab initio* methods whose main characteristics will be briefly sketched.

The fact that electrons are indistinguishable and are Fermions requires that their wave functions must be antisymmetric when two electrons are permuted.

This leads to the phenomenon of exchange and correlation. There are two types of approaches for a full quantum mechanical treatment of many-particles systems: Hartree-Fock (HF) and Density Functional Theory (DFT). The traditional scheme is the HF method which is based on a wave function in a form of one single Slater determinant. Exchange is treated exactly but correlation effects are neglected. The latter can be included (via the inclusion of several Slater determinants) by more sophisticated approaches such as configuration interaction (CI), but they progressively require much more computer time. As a consequence, it is only feasible to study small systems which contain a few atoms. An alternative scheme is DFT which is commonly used to calculate the electronic structure of complex systems containing many atoms such as large molecules or solids. DFT is based on the electron density rather than on the wave functions and treats both exchange and correlation, but both approximately. The ideal crystal is defined by the unit cell which may contain several atoms (up to about 100, in practical state-of-the-art calculations) and is repeated infinitely according to the translational symmetry. Periodic boundary conditions are used to describe this infinite crystal. The additional symmetry operations (inversion, rotation, mirror plane, etc.) that retain the ideal crystal invariant allow to simplify the calculations, which always correspond to the absolute zero temperature.

The details of the DFT method can be found in most general quantum physical or chemistry textbooks. The following is a brief introduction to the elementary concepts of the DFT method extracted from the textbook of Leach [30].

2.1 Density functional theory

Density functional theory is an approach to the electronic structure of atoms and molecules which has enjoyed a dramatic surge of interest since the late 1980s and 1990s [33, 34]. In DFT the wave function is constructed considering single-electron functions, but does not calculate the full N-electron wave function. DFT only attempt, is to calculate the total electronic energy (E) and the overall electronic density distribution ($\rho(\mathbf{r})$). The central idea underpinning DFT is that there is a relationship between the total electronic energy and the overall electronic density. This is not a particularly new idea; indeed an approximate model developed in the late 1920s (the Thomas-Fermi model) contains some of the basic elements. However, the real breakthrough came with a paper by Hohenberg and Kohn [35], who showed that the ground-state energy and other properties of a system were uniquely defined by the electron density. This is sometimes expressed by stating that the energy, E, is a unique *functional* of $\rho(\mathbf{r})$. In DFT the energy functional is written as a sum of two terms (equations are given in atomic units, unless otherwise stated):

$$E[\rho(\mathbf{r})] = \int V_{\text{ext}}(\mathbf{r})\rho(\mathbf{r})d\,\mathbf{r} + F[\rho(\mathbf{r})] \tag{2.1}$$

The first term arises from the interaction of the electrons with an external potential $V_{\text{ext}}(\mathbf{r})$ (typically due to the Coulomb interaction with the nuclei). $F[\rho(\mathbf{r})]$ is the sum of the kinetic energy of the electrons and the contribution from interelectronic interactions. The minimum value in the energy corresponds to the exact ground-state electron density, so enabling a variational approach to be used (i.e. the "best" solution corresponds to the minimum of energy and an incorrect density gives an energy above the true energy). There is a constraint on the electron density as the number of electrons (N) is fixed:

$$N = \int \rho(\mathbf{r})d\,\mathbf{r} \tag{2.2}$$

In order to minimize the energy we introduce this constraint as a Lagrangian multiplier ($-\mu$), leading to:

$$\frac{\delta}{\delta\rho(\mathbf{r})}\left[E[\rho(\mathbf{r})] - \mu\int \rho(\mathbf{r})d\,\mathbf{r}\right] = 0 \tag{2.3}$$

From this we can write:

$$\left(\frac{\delta E[\rho(\mathbf{r})]}{\delta\rho(\mathbf{r})}\right)_{V_{\text{ext}}} = \mu \tag{2.4}$$

Equation (2.4) is the DFT equivalent of the Schrödinger equation. The subscript V_{ext} indicates that this is under conditions of fixed external potential (i.e. fixed nuclear positions). It is interesting to note that the Lagrange multiplier, μ, can be identified with the chemical potential of an electron cloud for its nuclei.

The second landmark paper in the development of DFT was by Kohn and Sham [36]. They derived a set of equations to solve (2.1), analogous to the Hartree-Fock formulation, which included exchange and correlation effects and were not much more difficult to solve. The difficulty with Equation (2.1) is that the function $F[\rho(\mathbf{r})]$ is not known. Kohn and Sham suggested that $F[\rho(\mathbf{r})]$ should be approximated as the sum of three terms:

$$F[\rho(\mathbf{r})] = T_s[\rho(\mathbf{r})] + E_{\text{H}}[\rho(\mathbf{r})] + E_{\text{XC}}[\rho(\mathbf{r})] \tag{2.5}$$

where $T_s[\rho(\mathbf{r})]$ is the kinetic energy of a system of *non-interacting* electrons in orbitals $\psi_i(\mathbf{r})$ with the same density $\rho(\mathbf{r})$ as the real system, $E_{\text{H}}[\rho(\mathbf{r})]$ is the classical electron-electron Coulombic energy, and $E_{\text{XC}}[\rho(\mathbf{r})]$ contains contributions from exchange and correlation. The first term, $T_s[\rho(\mathbf{r})]$, in Equation (2.5), is given by:

$$T_s[\rho(\mathbf{r})] = \sum_{i=1}^{N} \int \psi_i(\mathbf{r}) \left(-\frac{\nabla^2}{2} \right) \psi_i(\mathbf{r}) d\,\mathbf{r} \tag{2.6}$$

The classical electron-electron Coulombic energy, $E_{\text{H}}[\rho]$, is also known as the Hartree electrostatic energy. Hartree [37] introduced this approach to solve the Schrödindger equation, but was almost immediately dismissed because it fails to recognize that electronic motions are correlated. In the Hartree approach this electrostatic energy arises from the classical interaction between two charge densities, which, when summed over all possible pairwise interactions, gives:

$$E_{\text{H}}[\rho(\mathbf{r})] = \frac{1}{2} \iint \frac{\rho(\mathbf{r}_1)\rho(\mathbf{r}_2)}{|\mathbf{r}_1 - \mathbf{r}_2|} d\,\mathbf{r}_1 d\,\mathbf{r}_2 \tag{2.7}$$

Combining these two and adding the electron-nuclear interaction, we can write the full expression for the energy of an N-electron system in the external potential due to M nuclei (with charge Z_A in positions $\mathbf{R}_A$). Hence, within the Kohn-Sham scheme:

$$\begin{aligned}E[\rho(\mathbf{r})] = &\sum_{i=1}^{N} \int \psi_i(\mathbf{r}) \left(-\frac{\nabla^2}{2}\right) \psi_i(\mathbf{r}) d\,\mathbf{r} + \frac{1}{2} \iint \frac{\rho(\mathbf{r}_1)\rho(\mathbf{r}_2)}{|\mathbf{r}_1 - \mathbf{r}_2|} d\,\mathbf{r}_1 d\,\mathbf{r}_2 \\ &+ E_{\mathrm{XC}}[\rho(\mathbf{r})] - \sum_{A=1}^{M} \int \frac{Z_A}{|\mathbf{r} - \mathbf{R}_A|} \rho(\mathbf{r}) d\,\mathbf{r} \end{aligned} \tag{2.8}$$

This equation acts to *define* the exchange-correlation energy functional $E_{\mathrm{XC}}[\rho(\mathbf{r})]$, which thus contains not only contributions due to exchange and correlation, but also a contribution due to the difference between $T[\rho]$, the true kinetic energy of the system, and $T_s[\rho]$. Therefore the exchange-correlation energy functional $E_{\mathrm{XC}}[\rho(\mathbf{r})]$ has the following expression:

$$E_{\mathrm{XC}}[\rho] = (T[\rho] - T_s[\rho]) + (E_{\mathrm{ee}}[\rho] - E_{\mathrm{H}}[\rho]) \tag{2.9}$$

Here, $E_{\mathrm{ee}}[\rho]$ is the true electron-electron interaction.

Kohn and Sham wrote the density $\rho(\mathbf{r})$ of the system as the sum of the square moduli of a set of one-electron orthonormal orbitals:

$$\rho(\mathbf{r}) = \sum_{i=1}^{N} |\psi_i(\mathbf{r})|^2 \tag{2.10}$$

By introducing this expression for the electron density and applying the appropriate variational condition the following one-electron Kohn-Sham equations result:

$$\left\{ -\frac{\nabla^2}{2} - \left(\sum_{A=1}^{M} \frac{Z_A}{|\mathbf{r} - \mathbf{R}_A|} \right) + \int \frac{\rho(\mathbf{r}_1)}{|\mathbf{r} - \mathbf{r}_1|} d\,\mathbf{r}_1 + V_{\mathrm{XC}}[\rho(\mathbf{r})] \right\} \psi_i(\mathbf{r}) = \varepsilon_i \psi_i(\mathbf{r}) \tag{2.11}$$

where ε_i are the orbital energies and V_{XC} is known as the exchange-correlation potential, related to the exhange-correlation energy by:

$$V_{\mathrm{XC}}[\rho(\mathbf{r})] = \left(\frac{\delta E_{\mathrm{XC}}[\rho(\mathbf{r})]}{\delta \rho(\mathbf{r})} \right) \tag{2.12}$$

The total electronic energy is then calculated from Equation (2.8).

To solve the Kohn-Sham equations, a self-consistent approach is taken. An initial guess of the density is fed into Equation (2.11) from which a set of orbitals can be derived, leading to an improved value for the density, which is then used in the second iteration, and so on until convergence is achieved.

2.1.1 Spin-polarized density functional theory

Local spin density functional theory (LSDFT) is an extension of "regular" DFT developed to deal with systems containing unpaired electrons. In this theory, both the total electron density (ρ) and the spin density (σ) are fundamental quantities with the spin density being the difference between the density of up-spin and down-spin electrons:

$$\sigma(\mathbf{r}) = \rho_{\uparrow}(\mathbf{r}) - \rho_{\downarrow}(\mathbf{r}) \tag{2.13}$$

The total electron density is just the sum of the densities for the two types of electron densities ($\rho = \rho_{\uparrow} + \rho_{\downarrow}$). The exchange-correlation functional is typically different for the two cases, leading to a set of coupled spin-polarized Kohn-Sham equations:

$$\left\{-\frac{\nabla^2}{2} - \left(\sum_{A=1}^{M} \frac{Z_A}{|\mathbf{r} - \mathbf{R}_A|}\right) + \int \frac{\rho(\mathbf{r}_1)}{|\mathbf{r} - \mathbf{r}_1|} d\,\mathbf{r}_1 + V_{\mathrm{XC}}[\mathbf{r}, \sigma]\right\} \psi_i^{\sigma}(\mathbf{r}) = \varepsilon_i^{\sigma} \psi_i^{\sigma}(\mathbf{r}) \qquad \sigma = \uparrow, \downarrow \tag{2.14}$$

This leads to two sets of wave functions, one for each spin, similar to spin-unrestricted Hartree-Fock (UHF) theory [38].

2.1.2 Local density approximation

The roots of DFT can be found in the works of Thomas [39] and Fermi [40] who independently studied the uniform electron gas in the early 1920s. The traditional Thomas-Fermi model is a first approximation to DFT in which the energy is a functional of the electronic density (of the uniform electron gas) solely. In the original work of Thomas and Fermi exchange and correlation were neglected, and was Dirac [41] who later introduced the exchange energy into the model (for a review see Refs. [42–45]). This suggests that in an inhomogeneous system, it may be possible to approximate the energy functional as an integral over a local function of the charge density.

After these works, it was clear that the exchange-correlation functional is the key to the success of the density functional approach. One reason why DFT is so appealing is that even relatively simple approximations to the exchange-correlation functional can give favorable results. The simplest way to obtain this contribution uses the so-called *local density approximation* (LDA; the acronym LSDA is also used, for local spin density approximation), which is based upon the model of the uniform electron gas, in which the electron density is constant throughout all space. Accordingly, the total exchange-correlation energy, E_{XC}, for our system can then be obtained by integration over all space:

$$E_{\mathrm{XC}}[\rho(\mathbf{r})] = \int \rho(\mathbf{r})\varepsilon_{\mathrm{XC}}^{\mathrm{unif}}(\rho(\mathbf{r}))d\,\mathbf{r} \tag{2.15}$$

$\varepsilon_{\mathrm{XC}}^{\mathrm{unif}}$ is the exchange-correlation energy per electron as a function of the density in the uniform electron gas. The exchange-correlation potential is obtained by differentiation of this expression:

$$V_{\mathrm{XC}}[\rho(\mathbf{r})] = \rho(\mathbf{r})\frac{d\varepsilon_{\mathrm{XC}}^{\mathrm{unif}}(\rho(\mathbf{r}))}{d\rho(\mathbf{r})} + \varepsilon_{\mathrm{XC}}^{\mathrm{unif}}(\rho(\mathbf{r})) \tag{2.16}$$

Thus, in the LDA it is assumed that at each point $\mathbf{r}$ in the inhomogeneous electron distribution (i.e. in the system of interest), where the density is $\rho(\mathbf{r})$, then $V_{\mathrm{XC}}[\rho(\mathbf{r})]$ and $\varepsilon_{\mathrm{XC}}(\rho(\mathbf{r}))$ have the same values as in the homogeneous electron gas. In other words, the real electron density surrounding a volume element at position $\mathbf{r}$ is replaced by a constant electron density with the same value as at $\mathbf{r}$. However, this "constant" electron density is different for each point in space.

The exchange-correlation energy per electron of the uniform electron gas is known accurately for all densities of practical interest from various approaches such as quantum Monte Carlo methods [46]. In order to be of practical use, this exchange-correlation energy density is then expressed in an analytical form that makes it amenable to computation. It is usual to express $\varepsilon_{\mathrm{XC}}(\rho(\mathbf{r}))$ as an analytical function of the electron density and to consider the exchange and correlation contributions separately. However, some analytical expressions for the combined exchange and correlation energy density also do exist, such as the expression of Gunnarsson and Lundqvist [47]. The relatively simple expression of Slater [48] is commonly used for the exchange-only energy under the LDA. In general, more attention has been paid to the correlation contribution, for which there is no such simple functional form. Perdew and Zunger [49] suggested a parametric relationship for the correlation contribution, which applies when the number of up spins equals the number of down spins and so is not applicable to systems with an odd number of electrons. The correlation energy functional was also considered by Vosko *et. al.* [50], whose expression has a very complex form.

2.1.3 Generalized Gradient Approximation

The most important feature of DFT is probably the way in which it directly incorporates exchange and correlation effects; the latter in particular are only truly considered in the more complex, post-HF approaches such as configuration interaction (CI) or many-body perturbation theory. Despite its simplicity, the LDA performs surprisingly well. However, the LDA has been shown to be clearly inadequate for some problems and for this reason extensions have been developed. The most common method is to use gradient-corrections, i.e. "non-local" functionals which depend upon the gradient of the density at each point in space and not just on its value only. These gradient corrections are typically divided into separate exchange and correlation contributions. A variety of gradient corrections have been proposed in the literature. One of the most widely used is the generalized gradient approximation (GGA). Several "flavors" within the GGA have been proposed and implemented in computational codes, some of them are: "PW86" (by Langreth and Perdew [51]), "PW91" (by Perdew and Wang [52, 53]), and "PBE" (by Perdew, Burke and Ernzerhof [54]), the latter being used in this work. The following is a description of the general GGA formulation, leading to the GGA-PBE approximation [54]. First, and as a rule, the exchange-correlation energy is separated in two terms, $E_{\mathrm{XC}} = E_{\mathrm{X}} + E_{\mathrm{C}}$, related to the densities of exchange (ε_{X}) and correlation (ε_{C}), respectively, and functionals containing the dependence with the gradient of the density. These contributions can in general be written as (in SI units):

$$E_{\mathrm{C}}[\rho_\downarrow,\rho_\uparrow] = \int \rho[\varepsilon_{\mathrm{C}}^{\mathrm{unif}}(r_s,\zeta) + H(r_s,\zeta,t)]d\,\mathbf{r} \tag{2.17}$$

$$E_{\mathrm{X}}[\rho_\downarrow,\rho_\uparrow] = \int \rho\varepsilon_{\mathrm{X}}F(s)d\,\mathbf{r} \tag{2.18}$$

where r_s is the local Seitz radius ($\rho = 3/4\pi r_s^3 = k_F^3/3\pi^2$), $\zeta = (\rho_\uparrow - \rho_\downarrow)/\rho$ is the relative spin polarization, and $t = |\nabla\rho|/2gk_s\rho$ and $s = |\nabla\rho|/2k_F\rho$ are dimensionless density gradients [55, 56]. Here $g(\zeta) = [(1+\zeta)^{2/3} + (1-\zeta)^{2/3}]/2$ is a spin-scaling factor [57], $k_s = \sqrt{4k_F/\pi a_0}$ is the Thomas-Fermi screening wave number ($a_0 = \hbar^2/me^2$), and $k_F = (3\pi^2\rho)^{1/3}$.
Perdew and coworkers proposed that H and F, in equations (2.17) and (2.18), should be constructed in such a way to fulfill certain "minimum" conditions to avoid over-parametrization. They construct the gradient contribution H from three conditions on the high- and low-density limits. Such conditions are fulfilled by the "simple" ansatz:

$$H = (e^2/a_0)\gamma g^3 \ln\left\{1 + \frac{\beta}{\gamma}t^2\left[\frac{1+At^2}{1+At^2+A^2t^4}\right]\right\}, \tag{2.19}$$

where

$$A = \frac{\beta}{\gamma}\left[\exp\left(\frac{-\varepsilon_{\mathrm{C}}^{\mathrm{unif}}}{\gamma\pi^3e^2/a_0} - 1\right)\right]^{-1} \tag{2.20}$$

where $\beta \simeq 0.066725$ and $\gamma \simeq 0.031091$. The exchange energy F is constructed from four further conditions, which are mainly concerned with the spin. Further information can be found in the literature [54].

2.1.4 van de Waals (vdW) functionals

Among the functionals explored for exchange and correlation, the vdW-DFT deserves particular attention, as it has proven to be superior as regards to electronic properties like the dipole moment and polarizability of some clusters [58, 59]. In the following is given a brief description taken from Aguado and coworkers [60, 61]. The vdW-DFT calculation corresponds to a first-principles approach based in the work of Dion and coworkers [62]. These authors demonstrated that the vdW interaction can be expressed by a nonlocal functional depending only on the electron density. After that work, numerous efforts have been developed to include vdW forces within DFT [63]. Dion and coworkers proposed to divide the exchange-correlation energy in three parts:

$$E_{\mathrm{XC}}[\rho(\mathbf{r})] = E_{\mathrm{X}}^{GGA}[\rho(\mathbf{r}), |\nabla[\rho(\mathbf{r})]|] + E_{\mathrm{C}}^{LDA}[\rho(\mathbf{r})] + E_{\mathrm{C}}^{nl}[\rho(\mathbf{r})] \tag{2.21}$$

where $E_{\mathrm{X}}^{GGA} = \int \rho(\mathbf{r})\varepsilon_{\mathrm{X}}^{GGA}[\rho(\mathbf{r}), |\nabla[\rho(\mathbf{r})]|]d\,\mathbf{r}$ is the exchange energy functional described through the semilocal generalized gradient approximation functional of Zhang and Yang [64], $E_{\mathrm{C}}^{LDA} = \int \rho(\mathbf{r})\varepsilon_{\mathrm{C}}^{LDA}[\rho(\mathbf{r})]d\,\mathbf{r}$ is the correlation energy described in the local density approximation of Perdew and Zunger [49], and E_{C}^{nl} is a nonlocal contribution to the correlation energy which contains the dispersion interaction, given by

$$E_{\mathrm{C}}^{nl}[\rho(\mathbf{r})] = \frac{1}{2}\iint \rho(\mathbf{r}_1)\,\phi(q_1, q_2, r_{12})\,\rho(\mathbf{r}_2)\,d\,\mathbf{r}_1 d\,\mathbf{r}_2 \tag{2.22}$$

where $r_{12} = |\mathbf{r}_1 - \mathbf{r}_2|$, and $q_1 = q(\mathbf{r}_1)$, $q_2 = q(\mathbf{r}_2)$ are the values of a universal function $q[\rho(\mathbf{r}), |\nabla[\rho(\mathbf{r})]|]$,

$$q[\rho, \nabla\rho] = \left[1 + \frac{\varepsilon_{\mathrm{C}}^{LDA}}{\varepsilon_{\mathrm{X}}^{LDA}} + \frac{0.8491}{9}\left(\frac{\nabla\rho}{2\rho k_F}\right)^2\right] k_F \tag{2.23}$$

The kernel ϕ has also a precise and universal form that in fact depends only on two variables, $d_1 = q_1 r_{12}$ and $d_2 = q_2 r_{12}$, but it can be written also as a function of q_1, q_2, and r_{12}. As a matter of fact, it is written in terms of $D = \frac{1}{2}(q_1 + q_2)r_{12}$ and $\delta = \frac{1}{2}(q_1 - q_2)r_{12}$, and then it can be shown that: (i) E_{C}^{nl} is strictly zero for any system with constant density; and (ii) the interaction between any two molecules has the correct r^{-6} dependence for large separations. Due to the high computational cost to self-consistently evaluate the E_{C}^{nl} term, applications of this functional are still scarce. Nevertheless, Román-Pérez and Soler have performed a very efficient self-consistent implementation of vdW-DFT functional in the SIESTA code [65], which allows to simulate large systems without significant extra cost as compared to LDA or GGA calculations.

3

Computational Procedure

3.1 SIESTA method

SIESTA (Spanish Initiative for Electronic Simulations with Thousands of Atoms) is an efficient linear scaling method to solve many electron systems based on the first principles DFT, following he $Kohn - Sham$ approach. It is also a computer code implementation whose distribution is under two main types of licenses depending in its use as academic or commercial, it also includes several auxiliary computer codes and post-processing tools. Further consulting of the method is found on reference [66]. Additional documentation and studies and applications of the method can be found on the following web addresses *http://www.uam.es/siesta* and *http://www.icmab.es/siesta*. The SIESTA method is the main tool for the present results of this thesis work.

In the next sections a brief explanation of some characteristics of the method are presented, mainly based on [67].

3.1.1 Basis set

The Kohn-Sham orbitals, ψ_ν, can be represented as a linear combination of a finite orbital base, ϕ_μ,

$$\psi_\nu = \sum_\mu c_{\nu\mu}\phi_\mu(\mathbf{r}). \tag{3.1}$$

The particular choice of the basis set functions characterizes the different numerical methods, some of such sets are: delocalized functions as plane waves, localized functions as Gaussians, a combination of both, and augmented basis. All approaches have their pros and cons, each of them offering different possibilities. Thus, the procedure is to select methodology and implementation adequate to correctly describe physical properties of the system under study.

SIESTA is a LCAO method (Linear Combination of Atomic Orbitals) which has a basis set composed by numerical atomic orbitals. Such orbitals correspond to the product of an spherical harmonic, Y_l^m, and a radial function, ϕ_{Iln},

$$\phi_\mu(\mathbf{r}) = \phi_{Iln}(r) Y_l^m(\theta, \varphi) \tag{3.2}$$

where I is the chemical species, l the angular moment, and n distinguishes the different wave functions with the same angular moment. The radial part depends only in the angular moment channel l, and the number of functions n used. Orbitals are strictly zero after a cutoff radius, r_c, this is done in soft manner to avoid noise in the force calculations.

The multiplicity introduced by n, or multiple-ζ following the quantum chemistry notation, is done to complete and improve the basis, obtaining better descriptions of the chemical bonding. This is done via a scheme named *split valence*. Additional orbitals with angular moment larger that the highest occupied orbital can be added, such *polarization orbitals* are used to better describe possible unbalances in the charges, as in covalent bonds. The most used basis is the DZP, or double(D)zeta(ζ)polarized(P) following standard nomenclature.

Locality of this kind of functions is important to efficiently construct the Hamiltonian, and in particular to the linear scaling of the numerical solution.

3.1.2 Pseudopotentials

Not all electrons in an atom behave in the same fashion to form a bond, some of them, the most inner ones, weakly (or virtually do not) take part in the bond. Electrons in the outermost shells have a larger probability to be found at interatomic distances, where their kinetic energy decreases to form the bond. Electrons near to the nucleus feel a very strong nuclear potential, being more localized, and their wave function overlap with electrons from neighbor atoms is tiny. Their main contribution is to *screen* the nuclear potential, thus modifying the wave functions of valence electrons.

This is the reason behind making a distinction between *external* (*valence*) and *inner* (*core*) electrons. Core electrons are treated as an effective potential which should produce the same wave functions for valence electrons from a certain *cutoff radius*. This effective potential is known as a *pseudopotential*, the basic idea was introduced by Fermi in 1934 [68]. The basic "recipe" for the distinction between core and valence electrons is whether they belong to a full or partially full shell, respectively. However, this should be carefully addressed for some chemical species, like transition metals and rare earths, where this approach gives poor results. In such situations it is necessary to include some of the innermost electrons as valence electrons, the so called *semi-core* electrons. Other corrections, such as a relativistic treatment, can be included depending on the chemical species under study.

There are several schemes for the construction of atomic pseudopotentials [69–75]. SIESTA uses norm-conserving Troullier-Martins pseudopotentials [75], in its fully non-local representation, as proposed by Kleinman and Bylander [76]. To obtain them, the *all electron* Hamiltonian is solved to obtain the wave functions of core and valence electrons. The potentials is adjusted to reproduce the valence orbitals outside the core radius of the orbital, and the process is repeated with this new potential. The use of pseudopotentials importantly lowers the computational cost, when carefully generated, one can obtain highly satisfactory results.

3.1.3 The Hamiltonian

The final Kohn-Sham Hamiltonian must contain the pseudopotential of the N atoms of the system substituting the true ionic potential

$$H^{KS} = \frac{p^2}{2m} + \sum_{i}^{M} \left[V_{NL}(\mathbf{r} - \mathbf{R}_i) + V_{NA}(\mathbf{r} - \mathbf{R}_i) \right] + V_H^{\delta}(\mathbf{r}) + V_{XC}(\mathbf{r}) \tag{3.3}$$

V_{NL} is the non-local term of the pseudopotential, V_{NA} is the potential of the neutral atom that contains the local part of the pseudopotential, V_H^{δ} is the *Hartree* potential created by a charge $\delta\rho(\mathbf{r}) = \rho(\mathbf{r}) - \rho_0(\mathbf{r})$ (the difference between the actual charge ρ, and the neutral atom charge ρ_0), and V_{XC} is the exchange-correlation potential.

The overlap matrix and the largest part of the Hamiltonian matrix elements are given by two-center integrals. Much of these elements become zero for local bases, thus giving the possibility of linear scaling. These elements are calculated in real or reciprocal space with Fourier techniques. The mesh distance in real space is given by a cutoff energy,

$$E_{cut} = \frac{1}{2}\frac{\pi}{\delta x} \tag{3.4}$$

where δx is the minimum distance between mesh points. This distance can be modified by a parameter called *mesh cutoff*. This is a precision parameter, the quality of the results depends on its value.

3.2 Computational details

In our DFT [77] SIESTA [66] calculations we have used the generalized gradient approximation as parametrized by Perdew, Burke, and Ernzerhof [54] for the exchange-correlation effects. We have used norm conserving scalar relativistic pseudopotentials [75] in their fully nonlocal form [76] with atomic valence configurations $3s^2 3p^2$ for Si (with core radii 1.9 a.u. for s and p orbitals), and $6s^2 5d^3$ for Ta (with core radii 3.2, 1.5 a.u. for the s and p orbitals, and a non-linear core correction radii of 1.0 a.u.). We have used a double-ζ polarized basis s, p for Si and s, d for Ta, with single polarization d for Si and p for Ta. For F we used the valence configuration $2s^2 2p^5$ with core radius 1.39 a.u. for all s, p, and d valence orbitals. For H the core radii are 1.25 a.u. for s and p orbitals. The integration in the k-space for the bulk calculations sc, bcc, fcc and NaCl cells was performed using a 4×4×4 Monkhorst pack grid [78]. For wires in the direction z we use a 1×1×6 Monkhorst pack grid. The basis set and pseudopotential of the Si and F atoms were used and tested before [79, 80]. Testings on the Ta pseudopotential are presented in section 4.1.

The equilibrium geometries result from an unconstrained conjugate-gradient structural relaxation using the DFT forces. The relaxation was stopped when the force on each atom was smaller than 0.01 eV/Å using a fineness of 250 Ry. Most of the initial geometries were taken from previous works due to Torres et. al. [81–83].

For the test on the accuracy we have taken two approaches (with the Ta@Si_{16}F system as a benchmark): (*i*) taking into account the Eggbox Effect (numerical noise in the integrals due to the finite mesh), (*ii*) by approximating the "infinite fine grid limit" (in which no Eggbox Effect would be present) at a Meshcutoff of 1000 Ry, and consider the system to be relaxed when the forces in the atoms are all less than 1 meV/Å; we conclude that: (*a*) the absolute error in the total energy is 0.005 eV, (*b*) the absolute error in the HOMO-LUMO gap is 0.002 eV, (*c*) the absolute error in the electric dipole is 0.03 Debye, and (*d*) the absolute error in the distances is 0.006 Å.

4

Tantalum doped Silicon clusters

$Ta^+@Si_n: \quad n = 14 - 18$

4.1 Tantalum pseudopotential

Here we present the tests on the Ta pseudoptential used in this work. For testing the Ta pseudopotential we have optimized the bulk bcc structure resulting in a cohesive energy of 8.30 eV, a lattice constant of 3.32 Å, and a bulk modulus of 187.75 GPa, to be compared with the experimental values [84] 8.09 eV, 3.31 Å, and 200 GPa, respectively. For the Ta_3 $\left(Ta_3^-\right)$ clusters we obtained from our spin-polarized calculations a C_{2v} (D_{3h}) symmetry, multiplicity 4 (5), and a first ionization potential of 0.96 eV, in agreement with a recent combined experimental and theoretical study [85]. For the bond lengths of Ta_3 $\left(Ta_3^-\right)$ we obtained 2.38 Å and 2.50 Å (2.42 Å), to be compared with 2.45 Å and 2.53 Å (2.46 Å) obtained by Wang and coworkers [85].

We also tested some other bulk structures besides the bcc for the Ta pseudopotential. Those tests confirmed our previous results: bulk bcc is the most stable structure for Ta. For the fitting of the Murnaghan curve [86] we made several calculations with different lattice constant in the bcc structure, then we used the DFT energies to fit them into a Murnaghan-type curve. In Table 4.1 we present a summary of the results obtained for the Ta pseudopotential, and in Figure 4.1 the Murnaghan fitting for the bcc structure.

Table 4.1: Ta, Ta_3, Ta_3^- electronic properties: the second column shows the results of the present work, the third column correspond to experimental data (energies are given in eV, distances are given in Å).

	Property	**This work**	**Experimental**
Ta	Electron affinity	0.08	0.32 [84]
	1st ion. pot.	7.49	7.89 [84]
	2nd ion. pot.	23.47	15.55 [84]
	Bulk modulus	185.75 GPa	200 GPa [84]
	Bulk structure	bbc (a=3.32)	bbc (a=3.30Å) [84]
Ta_3	Electron affinity	1.00	1.35 [85]
	symmetry	C_{2v}	C_{2v} [85]
	distances	2.38, 2.50	2.45, 2.53 [85]
	multiplicity	4	4 [85]
Ta_3^-	symmetry	D_{3h}	D_{3h} [85]
	distance	2.42	2.46 [85]
	multiplicity	5	5 [85]

4.2 Ta^+@Si$_n$ clusters (n=14-18)

In this section we present the results of the study of Ta^+@Si$_n$ clusters in the range $n = 14 - 18$, resulting at $n = 16$ in a positive peak for the second energy difference in the total energy [see equation (4.2) below], which is related directly to the higher abundance of that cluster found in mass spectrometry experiments. In order to explain the role of the impurity, we make a systematic study of the relative stability of Ta^+@Si$_n$ for $n = 14 - 18$. Accordingly to the experimental work of Nakajima and coworkers [25] we expect that for $n = 16$, the doped clusters will be more stable than its neighbors clusters.

Consequently for these doped clusters we will compare the binding (atomization, cohesive) energy per atom,

$$E_b(\mathrm{Si}_nM) = \left[E(M) + nE(\mathrm{Si}) - E(\mathrm{Si}_nM)\right]/(n+1), \tag{4.1}$$

the second difference of the cluster energy,

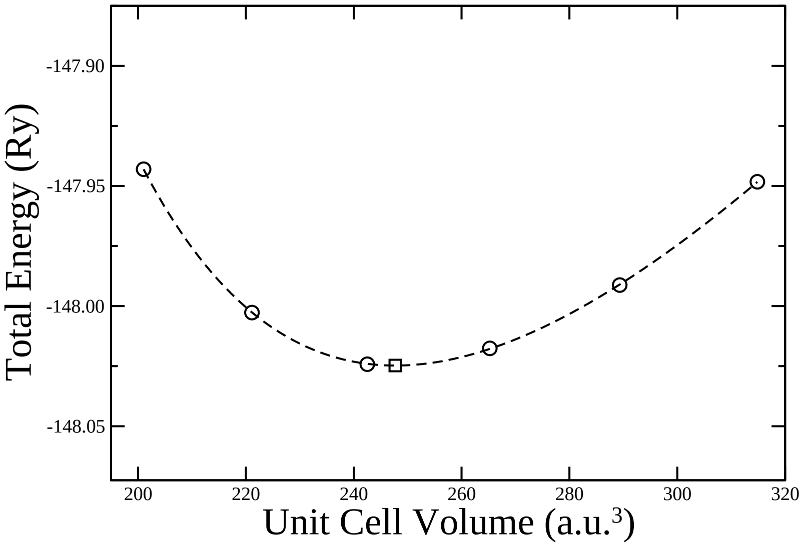

Figure 4.1: Murnaghan fit for the Ta pseudopotential used in this work in a bcc structure. The dashed line correspond to the fitting, circles represents data obtained by our calculations, and the square correspond to the equilibrium volume predicted by the fitting.

$$\Delta_2 E(\mathrm{Si}_n\mathrm{M}) = E(\mathrm{Si}_{n+1}\mathrm{M}) + E(\mathrm{Si}_{n-1}\mathrm{M}) - 2E(\mathrm{Si}_n\mathrm{M}), \tag{4.2}$$

and the energy difference between the eigenvalues of the lowest unoccupied (LUMO) and the highest occupied (HOMO) molecular orbital, $\Delta(H-L)$. In the expressions above $E(X)$ is the total energy of system X. The second difference energy $\Delta_2 E(\mathrm{Si}_n\mathrm{M})$ is proportional to $\log(I_n/I_{n+1})$, where I_n is the intensity of the MSi$_n$ signal in the experimental mass spectra. Therefore $\Delta_2 E$ is directly related to the abundance spectra.

The equilibrium geometries of a few low-lying energy isomers of isoelectronic Ta$^+$@Si$_n$ clusters are represented in Figures 4.2-4.7 for the sizes $n = 14-18$, and in Figure 4.8 is shown the evolution of several quantities – lower energy states only– with the cluster size n: binding energy per atom (or cohesive energy, as given by equation (4.1)), the second energy difference of the total cluster energy ($\Delta_2 E$, as given by equation (4.2)), and the HOMO-LUMO gap.

For the most stable geometries we can see that a common structural motif for lowest energy state structures of Ta^{+}@Si_n with $n = 14, 17, 18$, is a distorted hexagonal prism (DHP) of Si atoms surrounding the Ta impurity, with additional Si atoms and dimers decorating the lateral prism faces. That DHP motif resembles the structure C_s ground state and C_{2h} reported recently for $Si_{12}Ni$ [87]. DHP has eight faces –2 hexagons and 6 quadrilaterals as lateral faces–, eighteen edges, and twelve vertices;

4.2.1 Ta^{+}@Si_{14}

Figure 4.2 shows the first seven isomers of Ta^{+}@Si_{14}. The first four isomers have the DHP motif plus: (*i*) ground state: two silicons (dimer) in front of two adjacent quadrilateral faces; (*ii*) first excited state: two silicons in front of opposite quadrilateral faces; (*iii*)second excited state: two silicons, one in front of a hexagonal face, one on a quadrilateral; (*iv*)third excited state: two silicons (dimer) on a hexagonal face. One should also note that 14-V has a structure that much resembles that of 16-III, a fullerene like structure. Finally the last two structures show a basket-like open structure being much less stable than the closed ones.

4.2.2 Ta^{+}@Si_{15}

A few low-lying energy isomers of Ta^{+}@Si_{15} are represented in Figure 4.3. Structure 15-I is made of triangular, square, and pentagonal faces, and has no DHP motif. Structure 15-II shows a little more open structure, but the Ta atom still remains inside the cage. Structures 15-III and 15-IV do have the DHP motif. 15-III has three silicons (triangular trimer) on a single square face of the DHP, just like 14-I with an additional Silicon. 15-IV has three silicons (linear chain) on a hexagonal face of the DHP. For this size these first four isomers have the same structure as V^{+}@Si_{15}), as found by Torres et al [81].

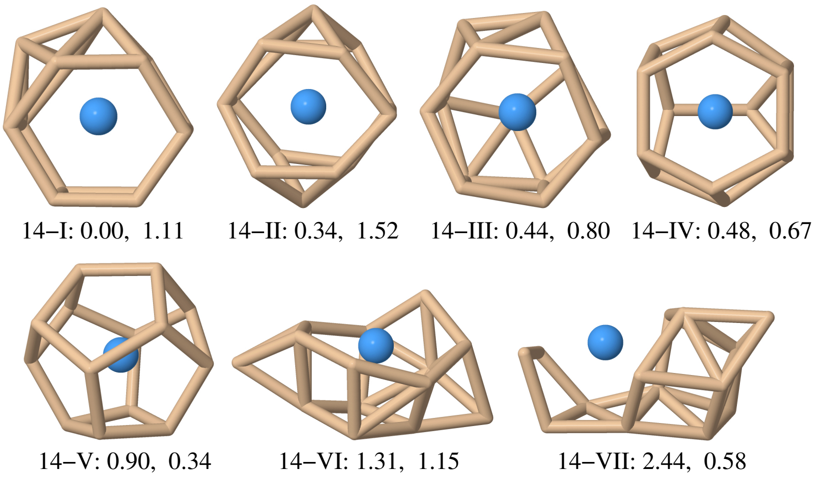
14–I: 0.00, 1.11
14–II: 0.34, 1.52
14–III: 0.44, 0.80
14–IV: 0.48, 0.67
14–V: 0.90, 0.34
14–VI: 1.31, 1.15
14–VII: 2.44, 0.58

Figure 4.2: Geometry of the first seven lowest energy isomers of Ta^{+}@Si_{14} clusters. The index I in 14-I indicates the different geometries, and corresponds to the order of the excited state, I being the lowest energy state, the next two numbers are the total energy difference and the HOMO-LUMO gap (both in eV).

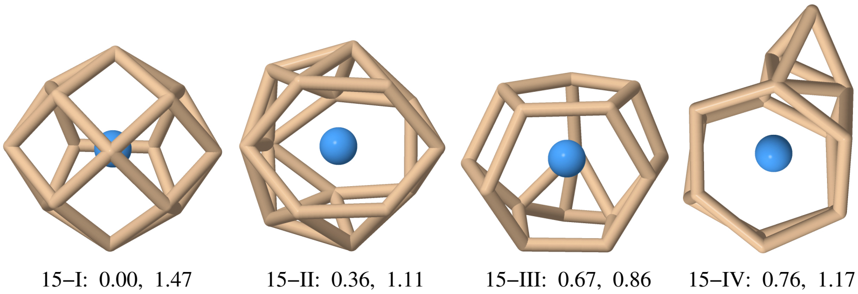
15–I: 0.00, 1.47
15–II: 0.36, 1.11
15–III: 0.67, 0.86
15–IV: 0.76, 1.17

Figure 4.3: Geometry of the first four lowest energy isomers of Ta^{+}@Si_{15} clusters. The index I in 15-I indicates the different geometries, and corresponds to the order of the excited state, I being the lowest energy state, the next two numbers are the total energy difference and the HOMO-LUMO gap (both in eV).

4.2.3 Ta^{+}@Si_{16}

The first four low-lying energy isomers of Ta^{+}@Si_{16} are represented in Figure 4.4. The ground state 16-I is a distorted Frank-Kasper polyhedron (FK*), this structure is nearly spherical and has a C_{3v} symmetry found by Kumar et al. [2]. It consists of a central Ta atom surrounded by 16 Si atoms within two closely spaced shells: one with 12 atoms (on the vertexes of an hexagonal antiprism with the dopant in the center), and another shell with 4 Si atoms forming a perfect tetrahedron. 16-II is a distortion of the ground state, in which the front triangle has been rotated, this rotation deforms the hexagonal antiprism.

Isomer 16-III is a fullerene-like (f) structure, which is also nearly spherical and has a D_{4d} symmetry; it consists of a central Ta with 16 Si atoms surrounding it, forming two square and eight pentagonal faces; each Si atom is coordinated with another three Si atoms. 16-IV is just like 15-I plus one Silicon.

Structures 16-I and 16-III densities of states are represented in Figure 4.5. They show the characteristic atom like shell structure, with a HOMO-LUMO gap of 2.44 and 1.77 eV, respectively. However, the splitting induced by the underlying geometry is different, especially for the projected density of Ta (d states) above the Fermi level. This fact should have measurable consequences in angle resolved x-ray spectroscopy [88].

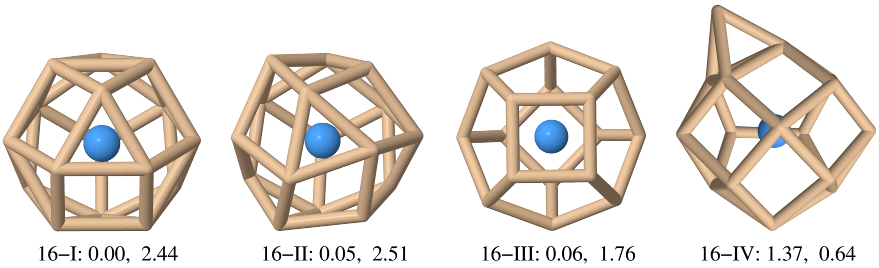

Figure 4.4: Geometry of the first four lowest energy isomers of $Ta^{+}@Si_{16}$ clusters. The index I in 16-I indicates the different geometries, and corresponds to the order of the excited state, I being the lowest energy state, the next two numbers are the total energy difference and the HOMO-LUMO gap (both in eV).

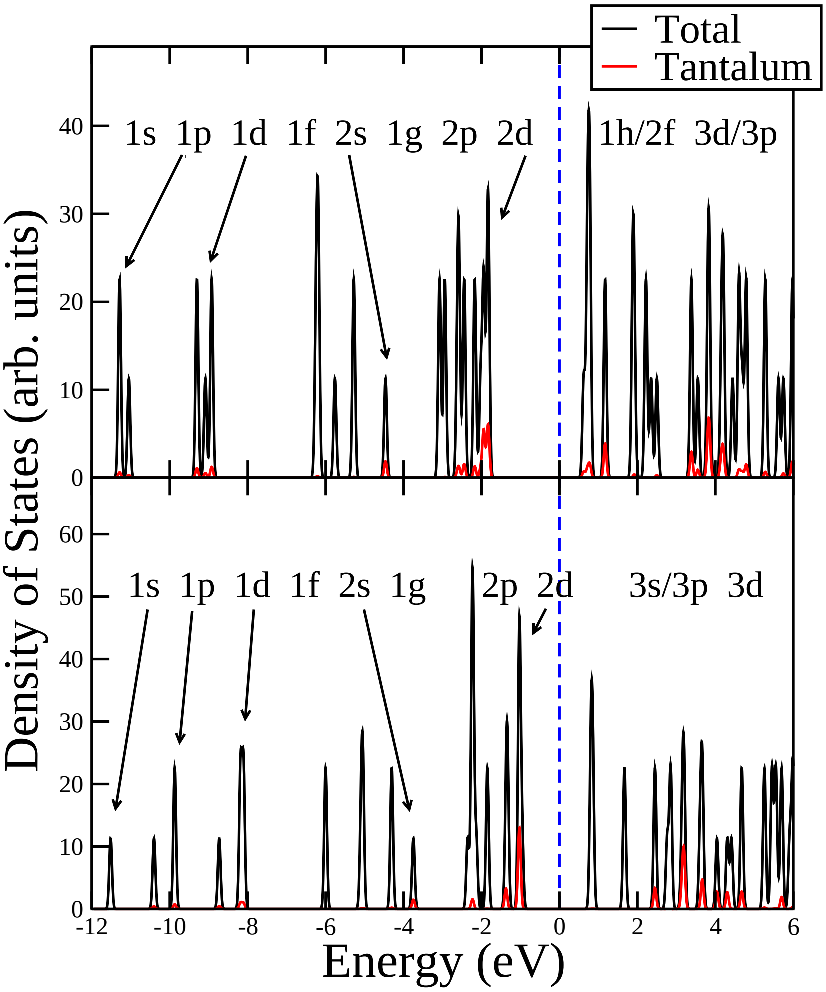

Figure 4.5: Total and Ta-projected density of states of C$_{3v}$ (upper) and D$_{4d}$ (lower) isomers of Ta$^+$@Si$_{16}$. The blue line indicates the Fermi level at zero energy. Here the notation for atomic spherical orbitals (nl) refers to the number of nodes (n) and to the orbital moment ($l : s = 0, p = 1, \ldots$)

4.2.4 Ta^+@Si_{17}

The results for Ta^+@Si_{17} in Figure 4.6 show that the lowest energy state is also a DHP with five Si atoms on an hexagonal face of the DHP. First and second excited states are made of the DHP plus a trimer and a dimer on its lateral (square) faces, but the dimer is in different orientations, with an energy difference of ~ 0.020 eV. Structures 17-IV and 17-V are semi-open structures with energies 0.322 and 0.788 eV higher than the ground state, respectively.

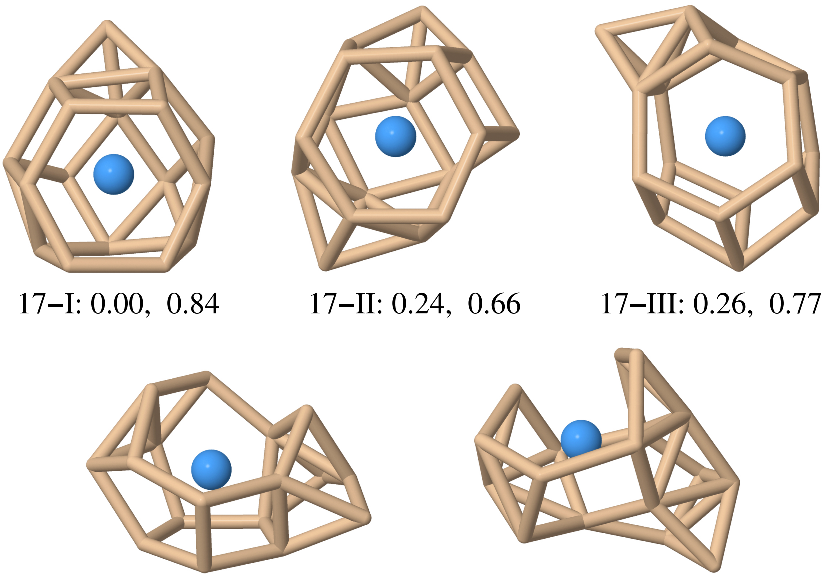

17–I: 0.00, 0.84 17–II: 0.24, 0.66 17–III: 0.26, 0.77

17–IV: 0.32, 1.06 17–V: 0.79, 1.15

Figure 4.6: Geometry of the first five lowest energy isomers of Ta^+@Si_{17} clusters. The index I in 17-I indicates the different geometries, and corresponds to the order of the excited state, I being the lowest energy state, the next two numbers are the total energy difference and the HOMO-LUMO gap (both in eV).

4.2.5 Ta^+@Si_{18}

The ground state is the DHP plus one Si, one Si_2, and one Si_3 in different faces of the DHP structure; while the Si goes a little bit inside the cage, the Si_2 and Si_3 go outside the cage. Structure 18-II is the DHP plus two Si_3 at opposite sides, the Ta is displaced from the center. Comparing with Vanadium [81] structures

18-I and 18-II exchange places (our 18-I for Ta is the first excited isomer for V, while our 18-II for Ta is the ground state for V). 18-III is the DHP plus three Si$_2$ on alternating square faces, 18-IV is the DHP plus six Si on one square face, 18-V is the DHP plus 2 Si$_3$ linear chain on both hexagonal faces. Finally 18-VI is an open structure.

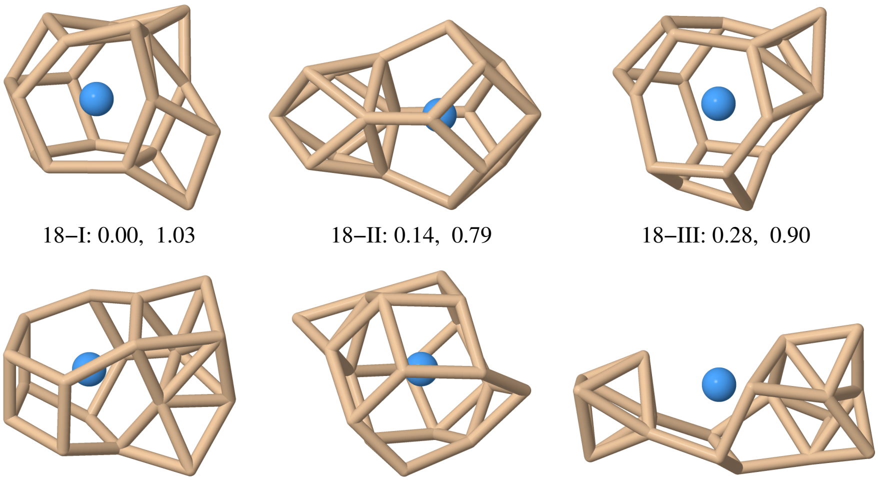

18–I: 0.00, 1.03

18–II: 0.14, 0.79

18–III: 0.28, 0.90

18–IV: 0.63, 0.42

18–V: 0.67, 0.96

18–VI: 1.23, 0.83

Figure 4.7: Geometry of the first six lowest energy isomers of Ta$^+$@Si$_{18}$ clusters. The index I in 18-I indicates the different geometries, and corresponds to the order of the excited state, I being the lowest energy state, the next two numbers are the total energy difference and the HOMO-LUMO gap (both in eV).

4.2.6 Trends in Ta$^+$@Si$_n$ $n = 14 - 18$

Figure 4.8 shows, for the lowest energy isomers of Ta$^+$@Si$_n$ clusters, the evolution with the cluster size n of several quantities: the binding energy per atom E$_b$, Equation (4.1), the second difference of the total cluster energy Δ_2E, Equation (4.2), and the energy difference between the LUMO and HOMO orbital eigenvalues, $\Delta(H - L)$.

For $n = 16$, the binding energy per atom, second energy difference of the total energy of the cluster, and the HOMO-LUMO gap show a peak for the nearly degenerated C_{3v} (Frank-Kasper polyhedron) and D_{4d} (fullerene-like) structures, the main difference being that the HOMO-LUMO gap of the C_{3v} structure is larger than the D_{4d} one. These facts according to the standard interpretation of the cluster mass spectra [24, 89], indicate a high abundance of $Ta^{+}@Si_{16}$ relative to their neighbor clusters. This agrees with the mass spectrometry experiments of Nakajima and co-workers [25].

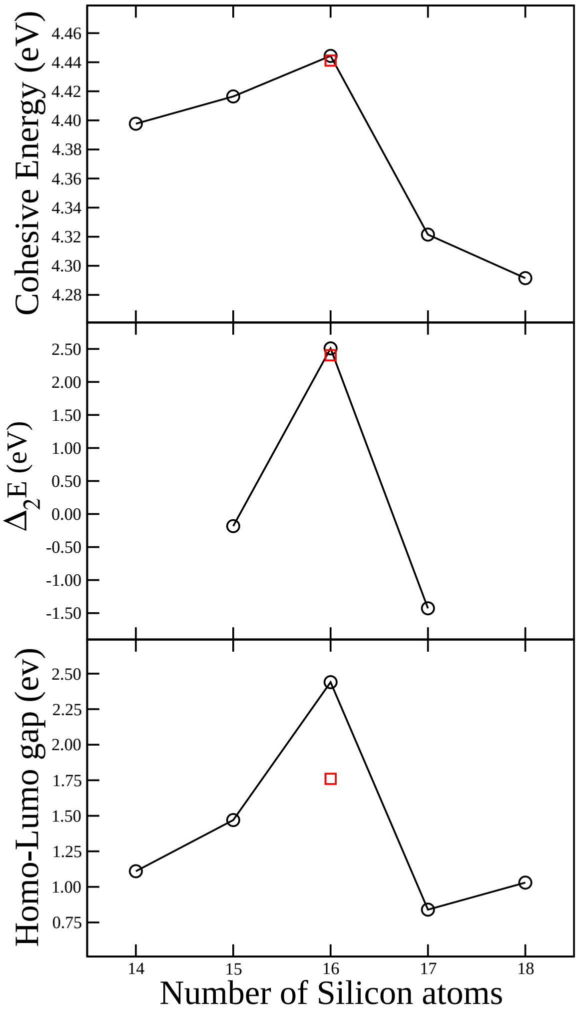

Figure 4.8: The panels from top to bottom represent, consecutively, the cohesive energy per atom, the second energy difference, and the HOMO-LUMO gap of the lowest energy state of Ta$^+$@Si$_n$ clusters as a function of the number of silicons n; the red square symbol at $n = 16$ represents the 16-III structure of Figure 4.4.

5

Ta@Si$_{16}$F: Aggregates

In order to assemble new materials containing metal-doped Ta@Si$_{16}$ clusters, we follow the suggestion of Nakajima and co-workers [25] considering neutral Ta@Si$_{16}$F as building blocks. First, we optimize the neutral Ta@Si$_{16}$ cluster geometry for both the C$_{3v}$ (Frank-Kasper polyhedron) and D$_{4d}$ (fullerene-like) geometries, with the result that the neutral D$_{4d}$ has 0.23 eV lower total energy than the C$_{3v}$ isomer; that is, the ordering of the neutral isomers changes with respect to that of the positively charged ones. In a second step we optimize Ta@Si$_{16}$F by considering different bonding sites of F on neutral Ta@Si$_{16}$ within the C$_{3v}$ and D$_{4d}$ symmetries, this is discussed in detail in section 5.1. As a third step we use the most stable Ta@Si$_{16}$F moiety we have found, fullerene like moiety, and use it to construct (Ta@Si$_{16}$F)$_m$ aggregates for $m = 2 - 6$ and 8; we study in detail their properties in subsections 5.2–5.7. In this chapter, our calculations are non spin polarized because that aggregates are non-magnetic, and we can save computational time for such larger compounds containing $\sim$ 100 atoms.

5.1 Ta@Si$_{16}$F

Taking into account the symmetry of the fullerene-like Ta@Si$_{16}$ (D$_{4d}$ symmetry) structure, it has: (*i*) 2 types of inequivalent faces (8 pentagons and 2 squares), (*ii*) 2 types of vertexes (those shared by two pentagons and square atoms [Si^1 atoms] and those shared by three pentagons [Si^2 atoms]), and (*iii*) 3 types of edges (those connecting two Si^1, those connecting two Si^2 atoms, and those connecting a Si^1 with a Si^2 atom).

The Frank-Kasper structure (C$_{3v}$ symmetry) has many more different available bonding sites for the F. From all the bonding sites the F atom prefers those in a top position, i.e. the F prefers to bond on the vertexes of either structure. Thus we have found six different Ta@Si$_{16}$F structures (altogether for the fullerene-like and Frank-Kasper polyhedron).

The ground state Ta@Si$_{16}$F cluster has the fullerene-like structure (16-III, Figure 4.4) plus a Fluorine atom in the line Ta-Si^1 ($\sim 2°$ deviated from this line), with a 5.15 Å Ta-F distance (see Figure 5.1), a binding energy per atom and a HOMO-LUMO gap of 4.18 eV and 1.44 eV respectively.
The next energy isomer is 0.37 eV above in total energy (1.47 eV HOMO-LUMO gap) and has the fullerene-like structure plus a Fluorine atom in the line Ta-Si^2 ($\sim 2°$ deviated from this line).
The FK-Ta@Si$_{16}$F most stable structure has 0.42 eV more total energy (2.03 eV HOMO LUMO gap) than f-Ta@Si$_{16}$F ground state (and only 0.040 eV more than the first excited state). f- and FK-Ta@Si$_{16}$F structures are shown in Figure 5.1.

While the HOMO LUMO gap of the most stable Ta@Si$_{16}$F structure is the smallest of the Ta@Si$_{16}$F structures, we would like to point out that it is well known that the Kohn-Sham HOMO-LUMO gap values, obtained from the corresponding eigenvalues of LDA-type or semilocal GGA-type functionals, severely underestimate the real gap values, which can be obtained (for finite systems) as the difference of the ionization potential (IP) minus the electron affinity (EA) calculated for the exact exchange-correlation functional [90]. When the gap values are estimated from the (IP-EA)$_{\text{calc}}$ values calculated with approximated LDA or GGA functionals, the mean absolute error (MAE) with respect to the experimental (IP-EA)$_{\text{exp}}$ values is reduced by an order of magnitude compared to the MAE resulting from ($\varepsilon^{\text{HOMO}} - \varepsilon^{\text{LUMO}}$) obtained with LDA or GGA Kohn-Sham calculations for a set of first row atoms and molecules [90]. The calculated IP and EA are 7.36 and 2.60 eV, respectively, for the D$_{4d}$ and 7.41 and 2.26 eV, for the C$_{3v}$ isomer of Figure 5.1 leading to an estimation of the gap of 4.76 for the D$_{4d}$ and 5.15 eV for the C$_{3v}$. These estimations are larger than the corresponding $\varepsilon^{\text{HOMO}} - \varepsilon^{\text{LUMO}}$ GGA values by a factor higher than 3.2. An accurate prediction of the fundamental gap of semiconductors has been given by a recent hybrid functional [91]. From Figs. 1–3 in that work [91] one can estimate correcting factors to the HOMO-LUMO GGA values in the ranges 1.5–1.1, 1.2–1.1, and 1.3–1.1 for one-, two-, and three-dimensional infinite semiconductor systems. Larger factors can be expected for finite semiconductor systems.

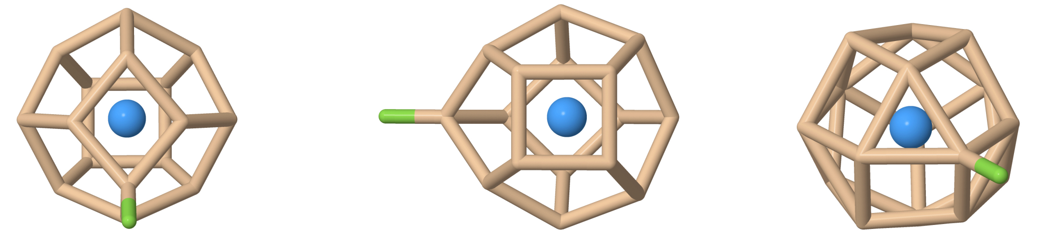

1–I: 4.18, 1.44, 1.74   1–II: 4.16, 1.46, 1.30   1–III: 4.16, 2.03, 2.21

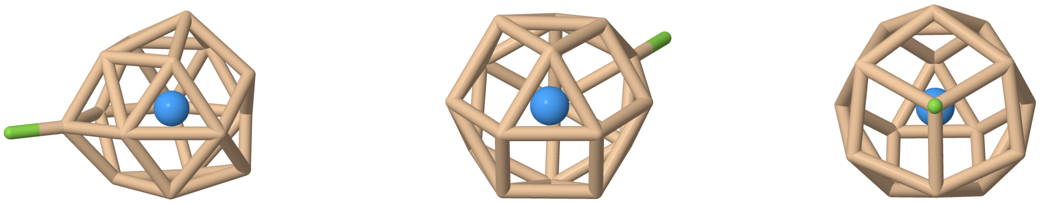

1–IV: 4.16, 2.03, 2.22   1–V: 4.16, 2.22, 2.04   1–VI: 4.13, 1.61, 2.43

Figure 5.1: Relaxed geometries for the Ta@Si$_{16}$F clusters. Below each structure are given: its label, binding energy per Ta@Si$_{16}$F unit (eV), HOMO-LUMO gap (eV), and dipole moment (Debye).

5.2 $\left(\mathbf{Ta@Si_{16}F}\right)_2$

From this section on, $Ta@Si_{16}F$ is the fullerene-like moiety (1-I) shown in Figure 5.1, and we define the binding energy per $Ta@Si_{16}F$ unit (E_b) of a $\left(Ta@Si_{16}\right)_n$ aggregate as follows:

$$E_b\left([Ta@Si_{16}]_n\right) = {}^1/_n\left[n \times E(Ta@Si_{16}) - E([Ta@Si_{16}]_n)\right].$$

We systematically search the $n = 2$ aggregates in order to select those isomers which can serve as unit blocks to construct larger aggregates following well defined patterns. By using the results with size $n = 2$, we study larger aggregates in the size range $n = 3 - 8$, later we further study the possibility of using certain configurations as unit cells of infinite low dimensional systems such as wires and nanotubes.

Figure 5.2 show the different configurations ordered by decreasing binding energy. In the lowest energy state, 2-I, three Si^1 and only one Si^2 participate in the bond between the two units. 2-II has the $Ta@Si_{16}F$ structures joined by two Si^1-Si^1 bonds, and the F atoms pointing in opposite directions, which leads to a nearly zero total dipole. Structure 2-III is basically the same as 2-II, the only difference being that the $Ta@Si_{16}F$ structures are rotated 90° around the line Ta-Ta, leading to a non-zero total dipole.

Structures 2-IV, 2-V, 2-VI, and 2-VII have the same pattern, in which the idea behind the motifs is that the units are joined by pentagonal faces (2-I and 2-III had also this motif before structural optimization). While 2-IV has four Si^1-Si^2 bonds, 2-V, 2-VI, and 2-VII share another common characteristic: the pentagonal faces involved in the bonding are “the same”, and they all have two Si^1-Si^1 and one Si^2-Si^2 bonds with the relative position of the F atom changing from one Si^1 to another. 2-VIII is a special case in which all bonds (four in total) are of the type Si^2-Si^2. 2-IX, 2-X, 2-XI, and 2-XII have only one Si^2-Si^2 bond, this seems to be the least favorable bonding type. 2-X and 2-XI bond types are observed in the bulk phase

What 2-V, 2-VI, and 2-VII in one hand and 2-IX, 2-X, 2-XI, and 2-XII on the other show us is the sensitivity of the binding energy of the systems. Special

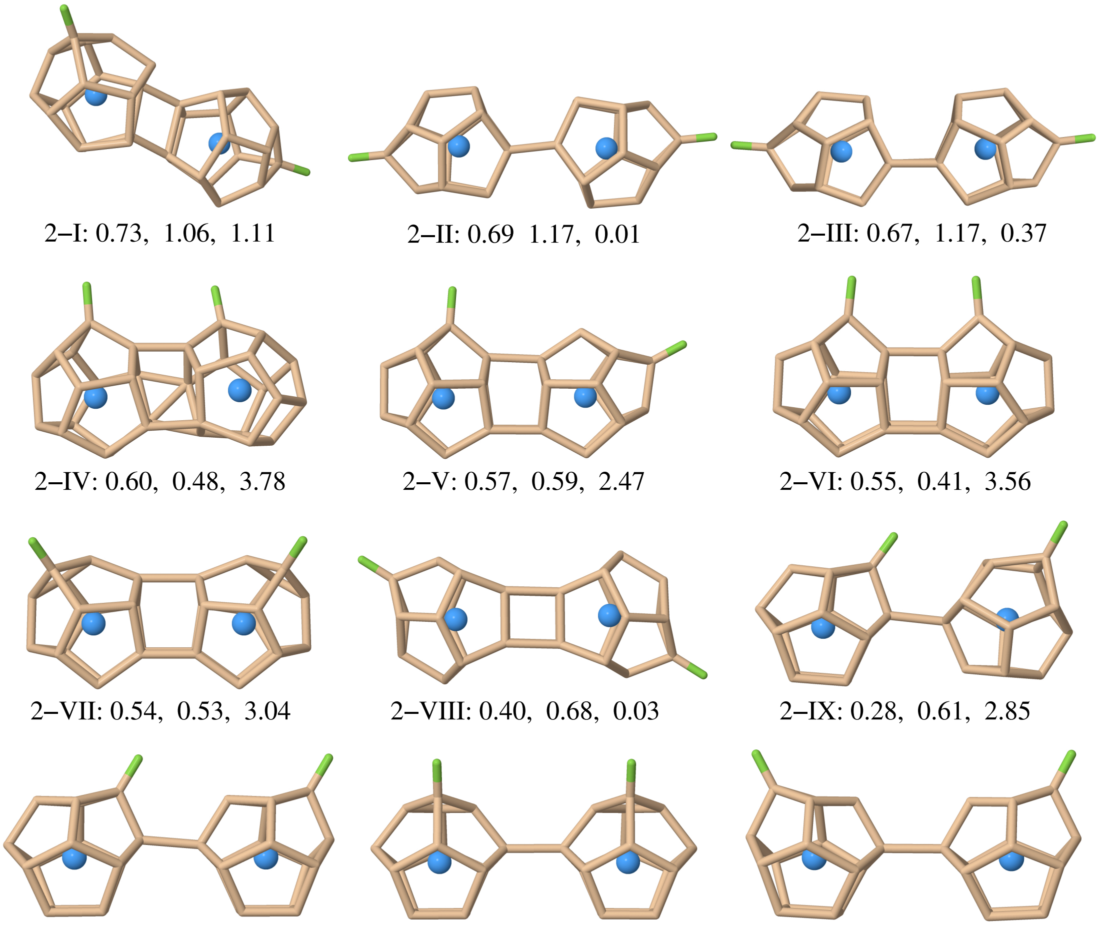

2–I: 0.73, 1.06, 1.11
2–II: 0.69 1.17, 0.01
2–III: 0.67, 1.17, 0.37
2–IV: 0.60, 0.48, 3.78
2–V: 0.57, 0.59, 2.47
2–VI: 0.55, 0.41, 3.56
2–VII: 0.54, 0.53, 3.04
2–VIII: 0.40, 0.68, 0.03
2–IX: 0.28, 0.61, 2.85
2–X: 0.24, 0.68, 2.86
2–XI: 0.22, 0.78, 3.49
2–XII: 0.20, 0.77, 3.24

Figure 5.2: Same as Figure 5.1 for $(\mathrm{Ta@Si_{16}F})_2$.

attention should be paid to 2-V and 2-VII (2-X and 2-XI), because such motifs are repeated in larger clusters with the same behavior of the binding energy with respect to the change in the dipole.

5.3 (Ta@Si$_{16}$F)$_3$

For the case (Ta@Si$_{16}$F)$_3$ several triangles and chains were tested, the preferred configuration for this size is the triangle. Among the first five more stable configurations four are triangles, and only one a (bended) chain. The ground state 3-I has the same triangular motif as 3-II, but 3-I Ta@Si$_{16}$F units become distorted after relaxation. The structure 3-II can be seen as the 2-III dimer of Figure 5.2 plus a Ta@Si$_{16}$F unit in such a position that the three square faces see each other, forming a hexagonal prism. That is, there are two Si^1-Si^1 bonds between each two Ta@Si$_{16}$F units. The 3-III isomer is nearly degenerate with the 3-II one (which has only 10 meV larger total energy) and can be seen as one half of an hexagon. It could be formed by breaking two Si^1-Si^1 bonds between two units and allowing a Si^2-Si^2 bond between each two units. Despite the nearly identical total energy of these isomers, the barrier for the 3-II to 3-III structural transition could be very large. The hardness IP$-$EA (see page 34) for the structures 3-II and 3-III is 2.51 and 2.40 eV, respectively, a factor $\sim$ 6.2 larger than the corresponding HOMO-LUMO gap values. The structure 3-III is a bended chain or also can be seen as half of the hexamer 6-III. 3-III is fairly degenerated with 3-II, despite of the different adopted geometries of each one. Structure 3-IV differs from that of the 3-II isomer in that one of the Ta@Si$_{16}$F units has been rotated 180° around a planar axis, resulting in more symmetrical relative bonding sites of the three F atoms, and, thus, a smaller dipole moment. The 3-V isomer is formed by choosing the Si^1 bonding sites of F to form a triangle in a different and parallel plane to the triangle formed by Ta atoms, which leads to a smaller binding energy per Ta@Si$_{16}$F unit (compare with 2-V and 2-VII of Figure 5.2).

Structures 3-VI and 3-VII can be seen as 2-II plus an Ta@Si$_{16}$F, these structures get dimerized and do not form a (Ta@Si$_{16}$F)$_3$, thus can not be used as basis motif for further larger aggregates. 3-VIII, 3-IX ,and 3-X share the same linear chain motif, with one Si^2-Si^2 bond between Ta@Si$_{16}$F units, they differ one from the other in the orientation of the Ta@Si$_{16}$F central unit. As opposed with 3-IV and 3-V (or 2-V and 2-VII) no positive nor negative correlation can be seen between the dipole and the binding energy among these isomers, i.e. for the linear chains, small dipole does not means lower binding energy nor the contrary.

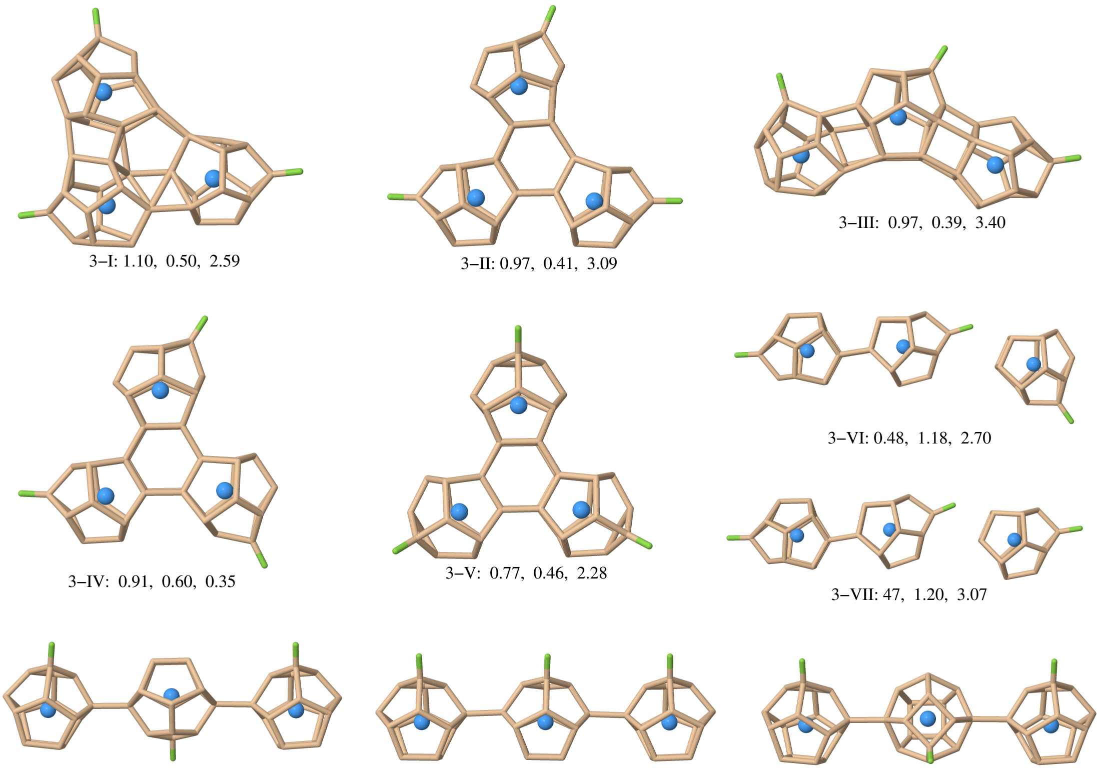

3–I: 1.10, 0.50, 2.59

3–II: 0.97, 0.41, 3.09

3–III: 0.97, 0.39, 3.40

3–IV: 0.91, 0.60, 0.35

3–V: 0.77, 0.46, 2.28

3–VI: 0.48, 1.18, 2.70

3–VII: 47, 1.20, 3.07

3–VIII: 0.34, 0.39, 1.57

3–IX: 0.33, 0.36, 5.59

3–X: 0.32, 0.36, 4.14

Figure 5.3: Same as Figure 5.1 for (Ta@Si$_{16}$F)$_3$.

5.4 (Ta@Si$_{16}$F)$_4$

For the size $n = 4$ we can finally build three dimensional aggregates. Lowest energy state 4-I is a tetrahedron, with structure 3-IV as basis and an extra Ta@Si$_{16}$F unit on top of it. Units are joined by Si^1 atoms. The bond between units deforms the square face; the fullerene like structure is still appreciable, but distorted and the symmetry of each unit is lost.

Structure 4-II has each component unit on the corners of a rectangle with the Ta and F in two parallel planes, leading to a total dipole in the direction of the normal to the planes. It was constructed with two 2-VII units joined by the four "free" Si^1 atoms, thus "mirroring" the 2-VII unit. After relaxation these four Si^1 atoms deviates from their original positions, thus deforming the "bottom" of the four Ta@Si$_{16}$F units, which in turn rotate a little bit forming one new Si^2-Si^2 bond between the Ta@Si$_{16}$F units of the 2-VII structures (i.e. two additional

Si^2-Si^2 in total).
Structure 4-III has two 2-VIII units side by side and rotated 90° one from the other, it can be seen as a tetrahedron with an isosceles triangle as basis. After relaxation all Ta@Si$_{16}$F units get distorted but the symmetry remains unaltered, in the process four new Si^2-Si^2 bonds.
Structure 4-IV and 4-VI have each Ta@Si$_{16}$F unit in the corners of a square of side 7.30 Å (Ta-Ta distance). While 4-IV has the F and Ta in the same plane, 4-VI F atoms is in two different Si^1, alternating up and down from the tantalums plane. An hypothetical 14-IV* structure, like 4-IV in which the Ta's and F's are in different parallel planes can not be obtained, such an hypothetical structure evolves to 4-II after relaxation.

Structure 4-V is formed of a 2-III plus a 2-VIII* (an hypothetical structure which is a modification of 2-VIII, in which one F atom would change its place, in such a way that each Ta@Si$_{16}$F molecule would be the mirror one of the other, such structure would evolve to 2-III after relaxation).

4-VII is a modification of 4-V, in which the 2-VIII* unit is modified, in such a way that the square faces containing the F atom face each other, thus loosing the bonds between Si^2's of the bottom square face. Finally, 4-VIII and 4-IX are linear chains with one Si^2-Si^2 and Si^1-Si^1 bond between Ta@Si$_{16}$F units, respectively.

5.5 (Ta@Si$_{16}$F)$_5$

For structures (Ta@Si$_{16}$F)$_5$ we used the 4-II as basis motif plus another Ta@Si$_{16}$F in different positions, and directions. In the structure 5-I we have the additional Ta@Si$_{16}$F on top a square face (this is the one formed by the Si^1 near the F) at the long side of the 4-II. 5-II and 5-III are three-dimensional rectangular pyramids, having the extra Ta@Si$_{16}$F above the plane of the 4-II unit, the only difference is a slight different orientation of the extra Ta@Si$_{16}$F structures. This top Ta@Si$_{16}$F deforms the 4-II structure. 5-IV, 5-V, and 5-VI have the extra Ta@Si$_{16}$F structure in the short side of the 4-II rectangle, with the additional Ta@Si$_{16}$F in different orientations.

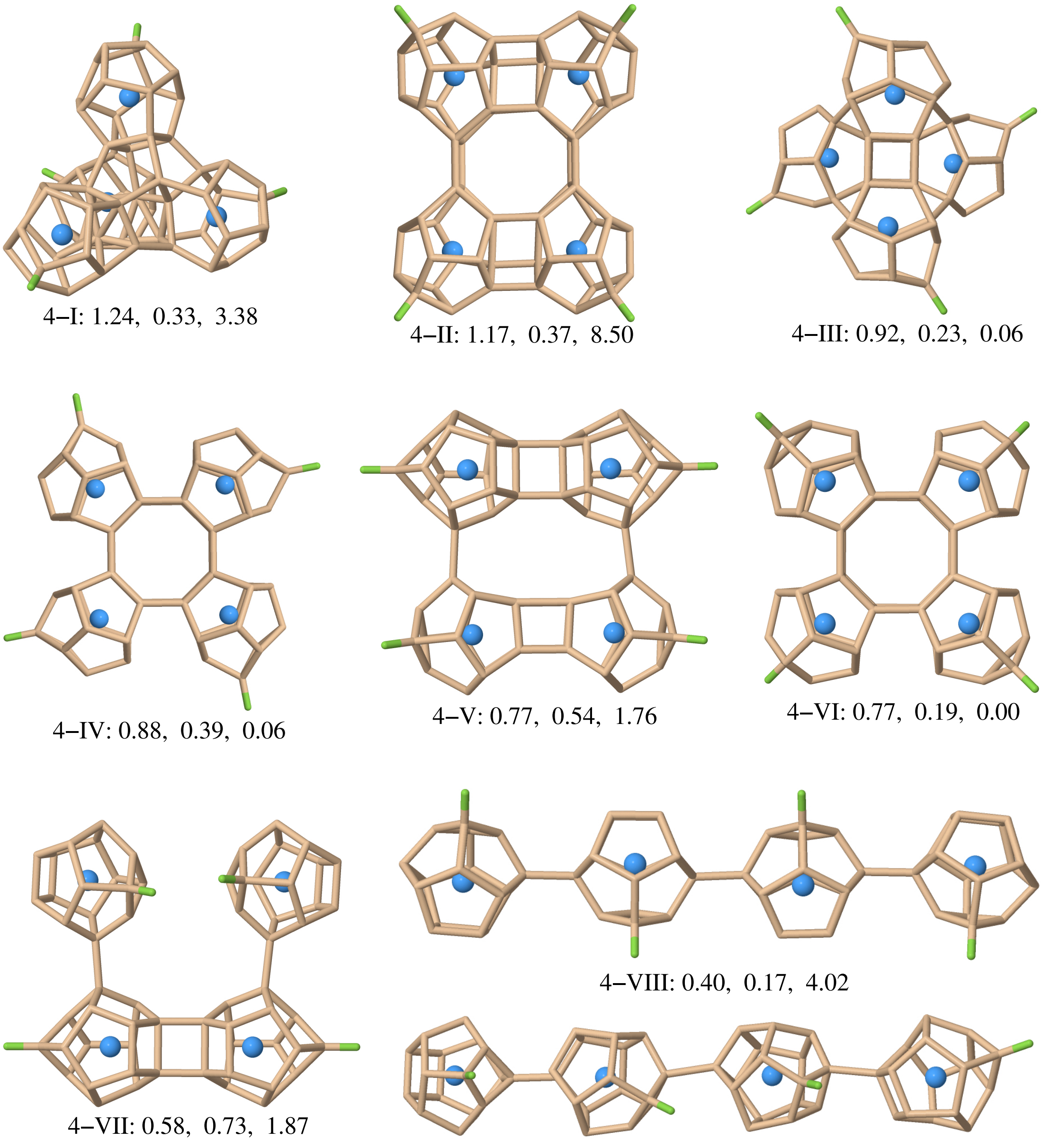

4–I: 1.24, 0.33, 3.38

4–II: 1.17, 0.37, 8.50

4–III: 0.92, 0.23, 0.06

4–IV: 0.88, 0.39, 0.06

4–V: 0.77, 0.54, 1.76

4–VI: 0.77, 0.19, 0.00

4–VII: 0.58, 0.73, 1.87

4–VIII: 0.40, 0.17, 4.02

4–IX: 0.35, 0.46, 3.52

Figure 5.4: Same as Figure 5.1 for ($Ta@Si_{16}F$)$_4$.

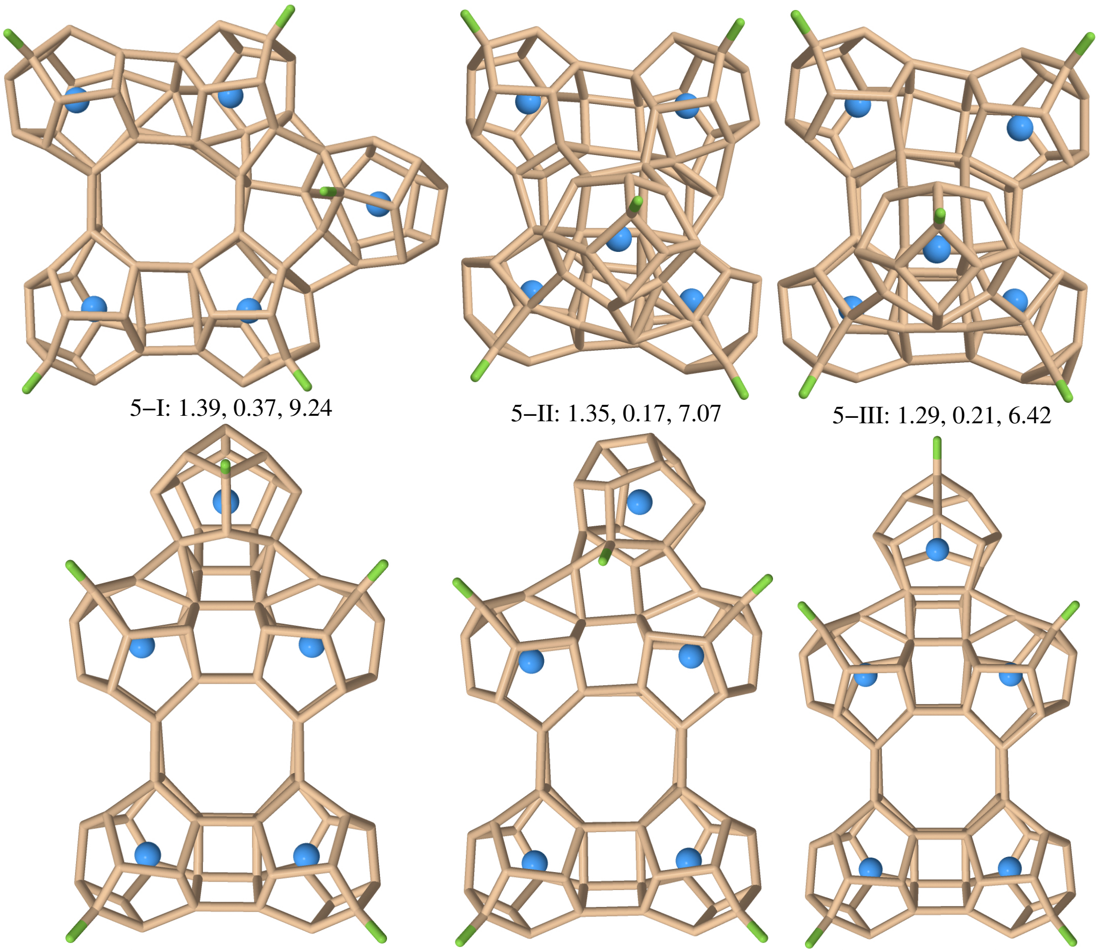

5–I: 1.39, 0.37, 9.24

5–II: 1.35, 0.17, 7.07

5–III: 1.29, 0.21, 6.42

5–IV: 1.28, 0.16, 8.91

5–V: 1.21, 0.28, 6.62

5–VI: 1.21, 0.25, 8.46

Figure 5.5: Same as Figure 5.1 for (Ta@Si$_{16}$F)$_5$.

5.6 $(\mathrm{Ta@Si_{16}F})_6$

The lowest-energy $(\mathrm{Ta@Si_{16}F})_6$ isomer which mantains the structure of the $\mathrm{Ta@Si_{16}F}$ units is shown in Figure 5.6 (6-I); it is formed from two 3-IV aggregates in two parallel planes and rotated 60° to each other around the vertical axis. Thus, the equilateral triangle formed by the three Ta atoms of the 3-IV isomer is stacked over the other similar triangle rotated by 60°. The structure 6-II, which is nearly degenerate with the 6-I one, can be seen as the stacking of two 3-V $(\mathrm{Ta@Si_{16}F})_3$ isomers rotated 60° one with respect to the other. The planar 6-III and 6-IV isomers in Figure 5.6 can be seen as the joining of three 2-V and 2-VII isomers, respectively, to form a ring (alternatively two 3-III units for the 6-III). The pair of isomers 6-I and 6-II (and 6-III and 6-IV) differs one from the other in the fluorine-bonding positions, illustrating again the sensitivity of binding energy and dipole moment to the fluorine relative bonding positions in the aggregates.

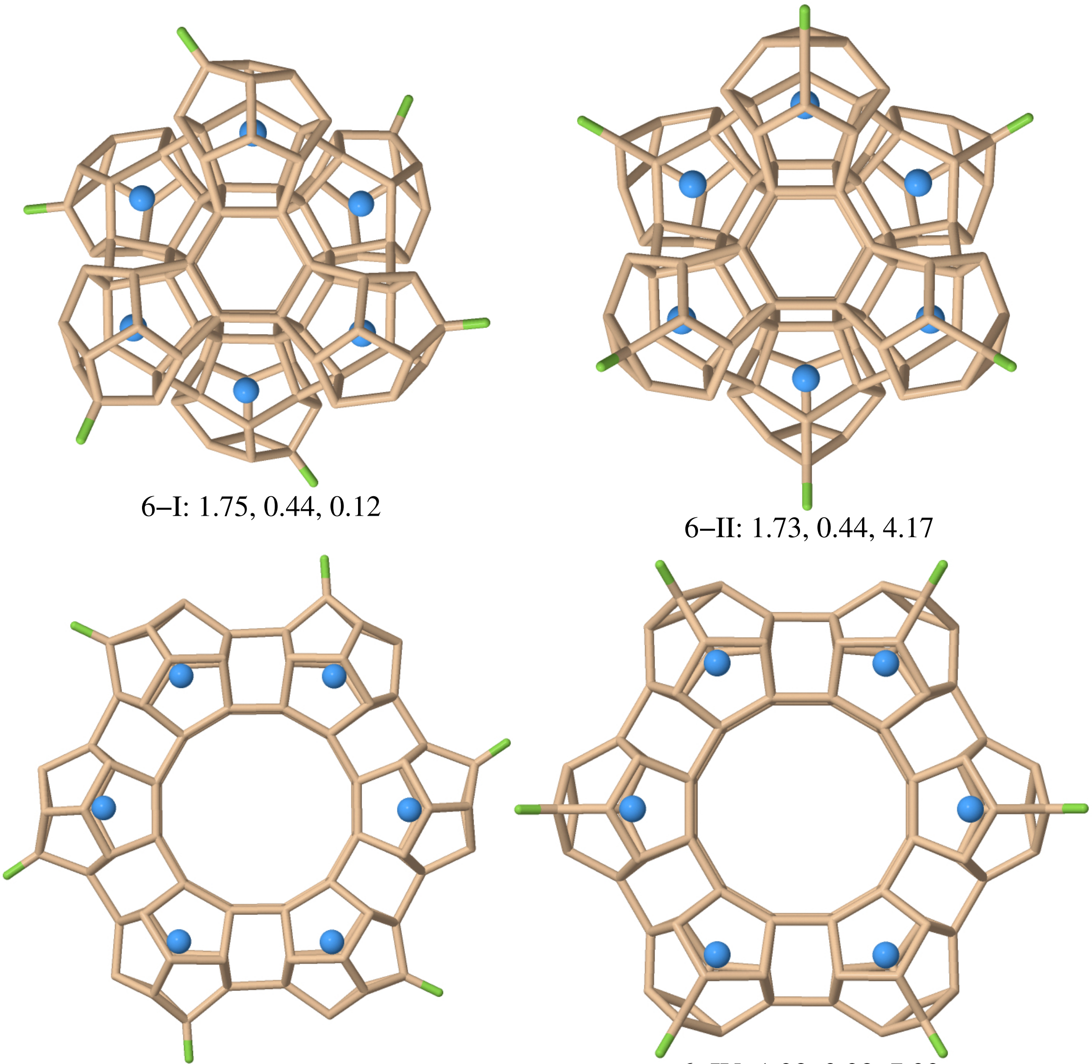

6–I: 1.75, 0.44, 0.12

6–II: 1.73, 0.44, 4.17

6–III: 1.45, 0.35, 0.01

6–IV: 1.38, 0.38, 7.32

Figure 5.6: Same as Figure 5.1 for (Ta@Si$_{16}$F)$_6$.

5.7 $(\mathrm{Ta@Si_{16}F})_8$

The 8-I isomer in Figure 5.7 is constructed by stacking two 4-IV isomers rotated 45° to each other around the vertical axis. The planar 8-II isomer is constructed by joining four 2-V units forming a ring, two additional $\mathrm{Si^2}$-$\mathrm{Si^2}$ bonds between $\mathrm{Ta@Si_{16}F}$ individual units are generated. These additional bonds deform the $\mathrm{Ta@Si_{16}F}$ units, and the fact that the $\mathrm{Si^1}$-$\mathrm{Si^1}$ bonds are more or less fixed with respect to the 2-VIII structure, "squeezes" the $\mathrm{Ta@Si_{16}F}$ units. These structures could be stacked vertically to create interesting nanotubes.

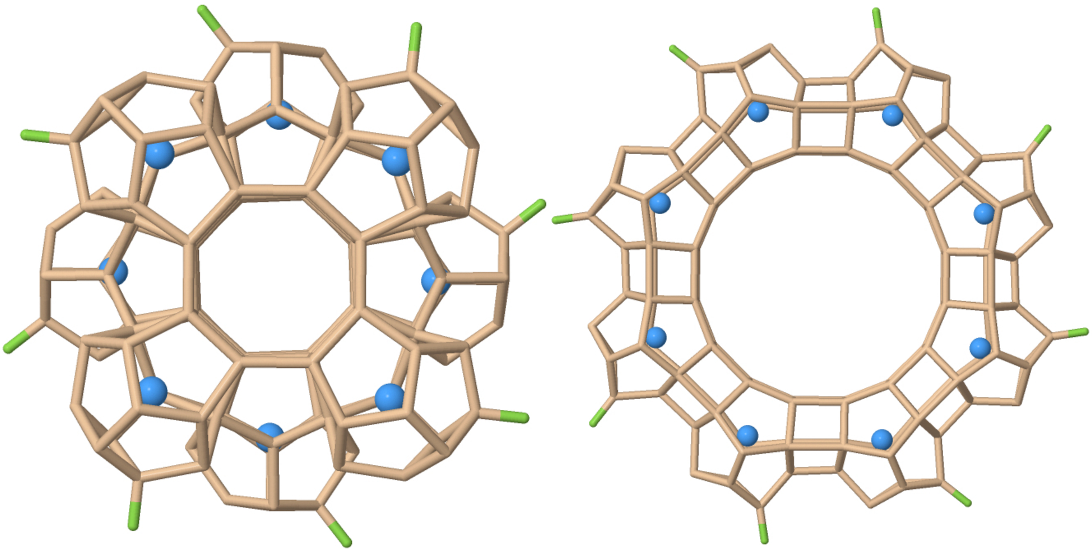

8–I: 1.67, 0.51, 0.15

8–II: 1.62, 0.21, 0.01

Figure 5.7: Same as Figure 5.1 for $(\mathrm{Ta@Si_{16}F})_8$.

6

Ta@Si$_{16}$F: Bulk phase

For possible stable bulk phases of Ta@Si$_{16}$F (fullerene-like moiety) molecular crystal we have tested the simple cubic, the face-centered cubic, and the NaCl structure. In all the cases no stable bulk phase could be found. However, in the case of a fcc-crystal with the $\mathrm{Ta}^{+} - \mathrm{F}^{-}$ electric dipole oriented along the crystallographic [110] direction a metastable phase could be identified. For the dipole oriented along [100] or along [111] the metastable phase disappeared. The metastable structure is shown in detail in Figure 6.1 has a cohesive energy of ~ 0.84 eV and lattice constant ~ 12.30 Å.

In all tested cases when the lattice constant becomes smaller than ~ 11.75 Å the cohesive energy increases drastically, and a strong deformation of the Ta@Si$_{16}$F unit is observed. Such deformations lead to amorphous bulk structures with silicon atoms of neighbor units bonding covalently. Panel (b) of Figure 6.2 shows a Murnaghan-Birch fit [86] to a few points around the local minimum, for both the energy and pressure. From that fit results a minimum at 12.273 Å with cohesive energy 0.836 eV, bulk modulus 7.55 GPa, and a phase stability pressure under isotropic compression smaller than 0.75 GPa.

The projected Si, Ta, and F density of states of bulk Ta@Si$_{16}$F, as well as the projected density of states of the 5d-orbital of Ta, are represented in panels (c) and (d) of Figure 6.2, respectively. We can see a small gap $\sim$0.20 eV between the 5d state of Ta, which are strongly hybridized with sp states of Si. A quick estimation of the correction factor can be obtained from our former discussion for Ta@Si$_{16}$F molecules. Thus using a correction factor of 2, a gap of ∼0.4 eV can be expected for the present case.

In order to study how unstable is that metastable fcc phase of Ta@Si$_{16}$F, we have performed $ab - initio$ annealing molecular dynamics (QAMD) at 300 K and constant volume. Panel (a) of Figure 6.3 shows the evolution of the energy difference with the starting zero-temperature energy along 4500 steps of molecular dynamics with 3×10^{-15}s per step, which amounts to a total time of 13.5 ps. We see that during the first 5 ps the total energy oscillates in the range ±0.4 eV around a given average value (-3363.80 eV). These oscillations reflect the relative orientations (rotations) driven by the covalent Si-Si interactions between neighboring cages. From 5 to 13.5 ps the total energy oscillates around an average value -3364.80, which is 1 eV smaller than the previous one. This fact suggests that the phase transition occurs due to changes in pressure, larger that those allowed by the fitted Murnaghan-Birch equation of the meta-stable state. In panel (c) of Figure 6.3 we can see that the pressure oscillates around 1.5 Mbar, a value out of the validity range of the fcc meta-stable state. Panel (b) of Figure 6.3 shows the evolution of the percent deviation of the Ta-Si$_b$ and Si$_b$-F bond lengths along the 13.5 ps annealing dynamics, where Si$_b$ is the silicon atom which connects Ta and F. That Si$_b$ is always the same as the initial one at 0 K. At 0 K the Si$_b$ atom forms a straight line with Ta and F atoms, with bond lengths 3.04 Å and 1.72 Å for Ta-Si$_b$ and F-Si$_b$ respectively. We see in panel (b) of Figure 6.3 that the distance Si$_b$-F remains approximately constant (within 0.2 %) along the 13.5 annealing dynamics. On the other hand the Ta-F and Ta-Si$_b$ distances follow a similar percent distance change evolution –compared one with the other– showing a drastic average value change starting at 5 ps.

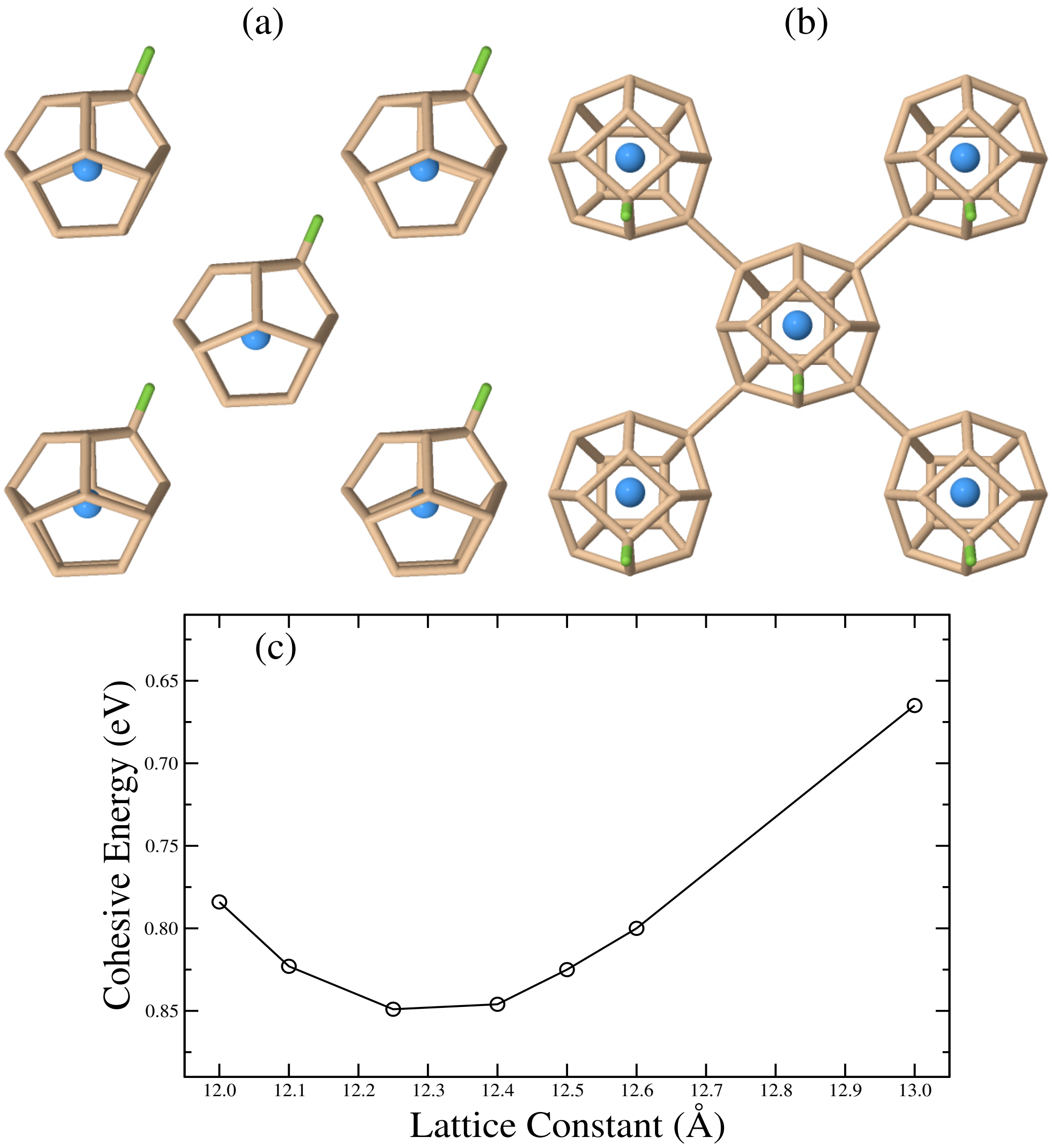

Figure 6.1: Panels (a) and (b) show the [100] and [001] planes, respectively, of the (Ta@Si_{16}F) in the fcc metastable phase, panel (c) shows the evolution of the cohesive energy against the first neighbor distance.

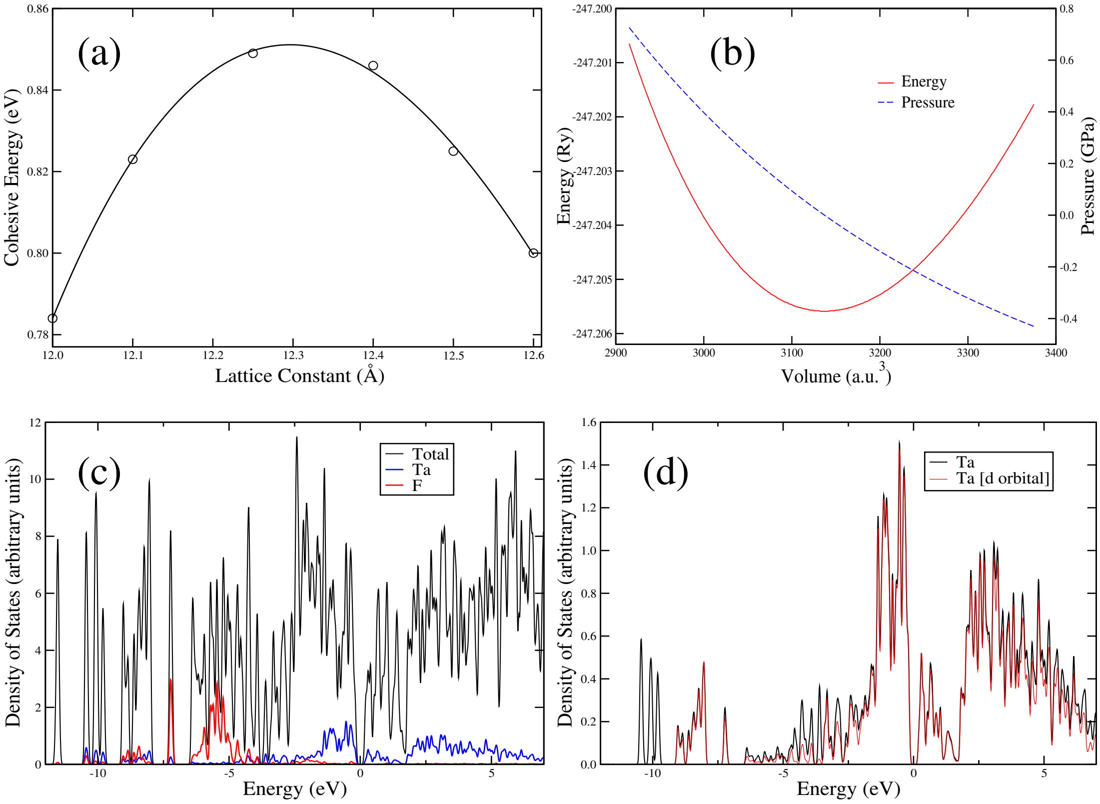

Figure 6.2: (a) Binding energy per unit cell of the metastable fcc Ta@Si$_{16}$F as a function of the lattice constant. (b) Murnahgan-Birch fit to the total energy and pressure of fcc Ta@Si$_{16}$F. (c) Total density of states and projected density of states of Ta and F atoms. (d) Projected DOS of Ta atom and of *d* states of Ta.

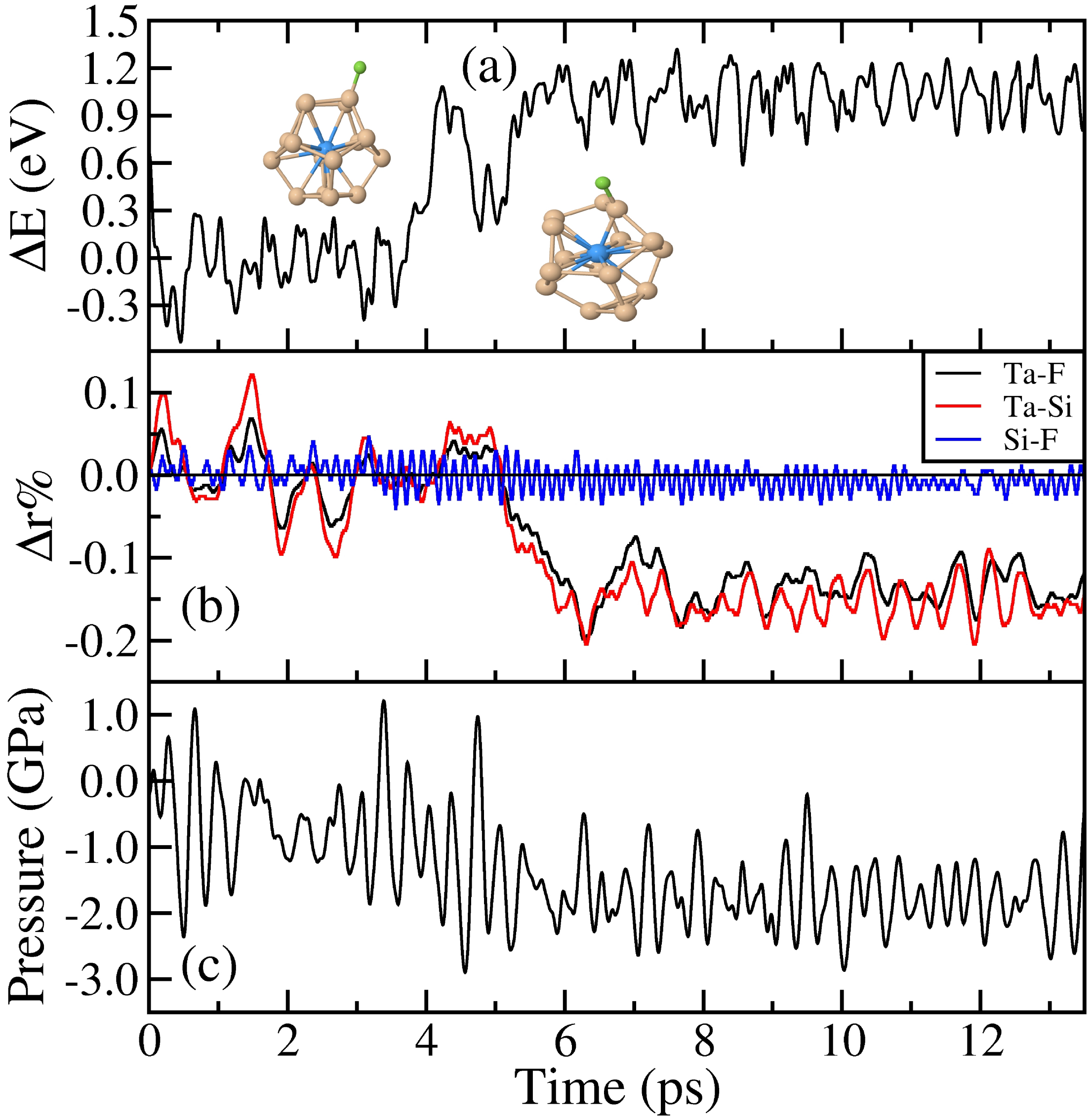

Figure 6.3: Evolution along 13.5 ps in the QAMD of (a) the cohesive energy difference of the bulk Ta@Si$_{16}$F metastable fcc phase at 300 K with the starting 0 K total energy [the insets show the Ta@Si$_{16}$F cluster in the unit cell before (left) and after (right) 5 ps]; (b) the distances Si$_b$-F (blue line), Ta-Si (red line), and Ta-F (black line); and (c) the total pressure in the cell.

7

$(\mathrm{Ta@Si_{16}F})_6$: Wire

We have used aggregate 6-I (see Figure 5.6) as a unit cell to construct an infinite wire. Figure 7.1 (a) and (b) show two units and top-view of the wire, respectively. The unit cell contains one 6-I aggregate (108 atoms) forming vertically an infinite wire which is separated laterally a distance 4L of similar wires in order to avoid interactions between them – where L is the distance between the first and third layers shown in Figure 7.1 (a).

The periodic calculations have been performed in a 4L × 4L × L parallelepiped cell. We use a k-grid cutoff of 15 Å to sample the Brillouin zone in reciprocal space, which corresponds to 125 k points. In Figure 7.1 (c) is represented the cohesive energy, defined as

$$E([\mathrm{Ta@Si_{16}F}]_6^{cluster}) - E([\mathrm{Ta@Si_{16}F}]_6^{wire}),$$

for different values of the lattice constant. The wire equilibrium state corresponds to L = 10.70 Å and a cohesive energy 1.87 eV.

The Mulliken population analysis [92] reveals that each $(\mathrm{Ta@Si_{16}F})_6$ unit conserves his nominal number of electrons (e), that is, 5(Ta) + 4 × 16(Si) + 7(F) = 76 e. Thus, 1.76 e are donated from the Ta 6s orbital to the Ta 6p orbital (0.46 e), to the Ta 5d orbital (0.64 e), to the 16 Si atoms (0.30 e), and to the F atom (0.36 e). This rearrangement of electrons between Ta, Si, and F corresponds qualitatively to their relative atomic electronegativity, and allows the formation of hybrid *spd* orbital of Ta in order to establish symmetry-adapted bonds with Si atoms.

A more detailed analysis leads to the conclusion that the charge neutralization occurs for each layer of atoms inside each supermolecular unit. These atomic layers are the following: (*i*) the F atom and those four Si^1 atoms which do not participate in the $Ta@Si_{16}F - Ta@Si_{16}F$ bonding; (*ii*) the eight Si^2 atoms in the equatorial zone between the two square faces having alternating excess/defect of nominal charge, thus neutralizing each pair of consecutive Si atoms; these eight Si^2 atoms are arranged in two parallel squares (45° twisted to each other) and the four atoms in a square have identical excess (or defect) of charge; (*iii*) the four Si^1 atoms of the square face which provide the bonding between adjacent cages; two of them bind covalently to another two Si^1 atoms of the other cage which have the same excess (trimer in the upper plane) or defect (trimer in the lower plane) of charge. There are also covalent Si^{2u}–Si^{2l} bonds between the upper plane and the lower plane.

It is interesting to characterize the empty space inside of the $(Ta@Si_{16}F)_6$ unit cell. In Figure 7.2 is depicted such a cage, which looks as a barrel delimited by 24 Si^1 atoms arranged in four parallel layers, each one with 6 atoms, whose vertical axis is the wire axis. The distance between layers is 2.17 Å , and between two consecutive holes is 4.19 Å . Each one of the 6 atoms in a layer has the same excess or defect of electrons. The surface density of positive/negative charge within each layer is nearly the same (-0.014 and $+0.016$ number of electrons per Å^2, respectively), and the cage can be seen as identical electrical capacitors opposed one to the other, that is, $(+,-)(-,+)$. The smallest (largest) “diameter” of the barrel is 4.88 Å (6.52 Å), and the height is 6.51Å ,which makes it possible to encapsulate small molecules as H_2, O_2, N_2, H_2O, etc.

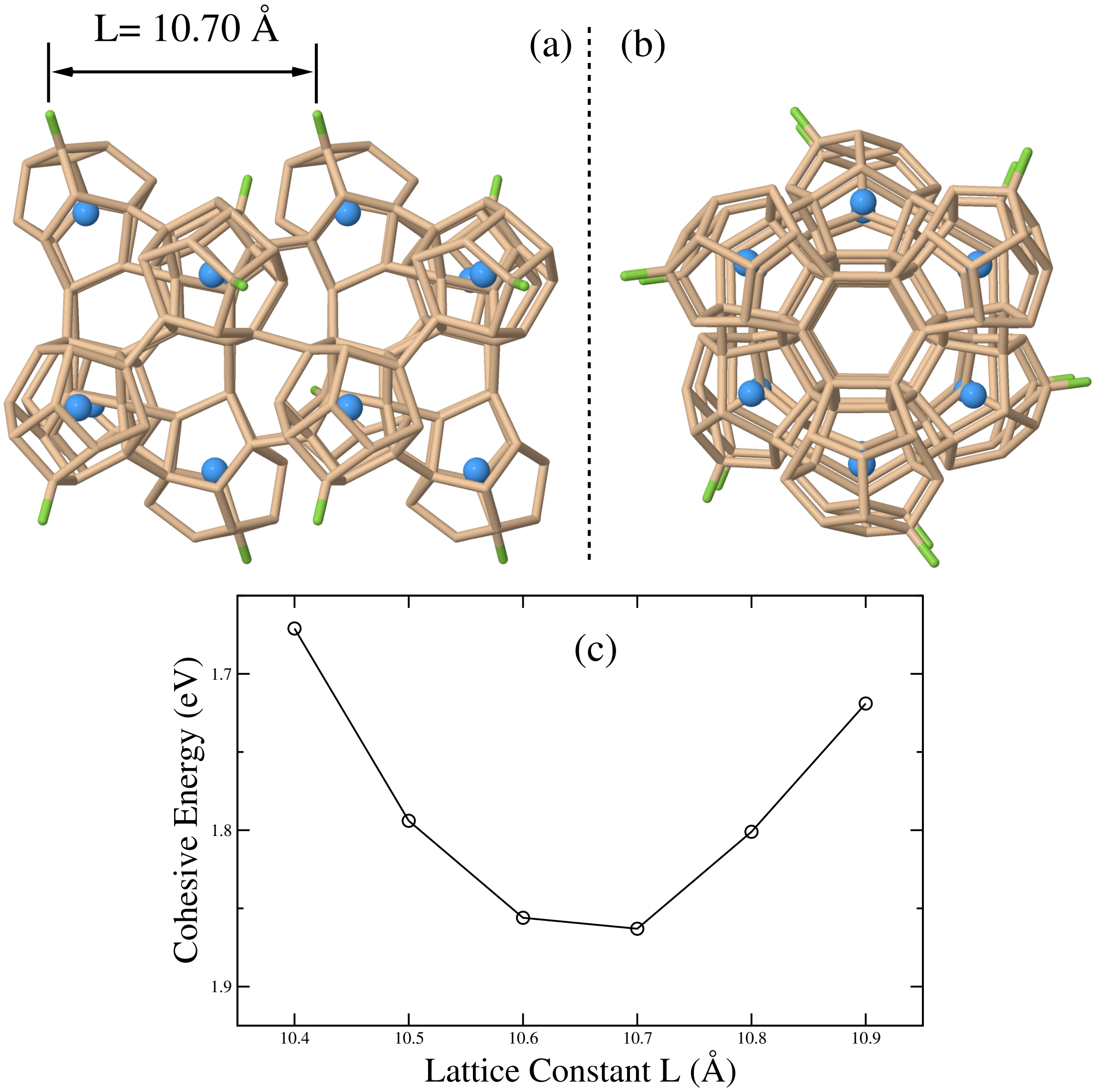

Figure 7.1: Panel (a) and (b) show the lateral and top views of a section of the wire containing two $(Ta@Si_{16}F)_6$ unit cells, indicating the lattice constant L. In panel (c) is represented the cohesive energy of the wire as a function of the cell distance L.

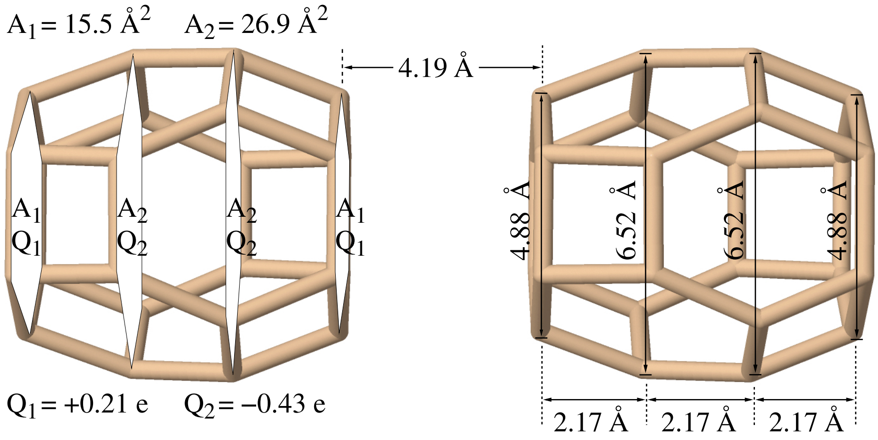

Figure 7.2: Size of the hole inside of the (Ta@Si$_{16}$F)$_6$ unit cell and number of electrons in the planes. The planes are perpendicular to the wire axis, and each one is formed by 3 pairs of Si^1 atoms.

8

Adsorption of small molecules on $Ta@Si_{16}F$, and $(Ta@Si_{16}F)_6$ clusters and wires

In the last section we have characterized a $(Ta@Si_{16}F)_6$ nanowire formed by two $(Ta@Si_{16}F)_3$ triangular aggregates stacked along the vertical axis and twisted 60° each other (Figure 7.1(a)), where the basic $Ta@Si_{16}F$ super-molecular unit has D_{4d} symmetry. The central cavity of the wire has a barrel shape formed by 24 Si atoms arranged in 4 parallel hexagons (Figure 7.2). The surface of that barrel is formed by 6 squares and 6 hexagons plus 2 hexagons as basis. Thus, following the notation used for clathrate hydrates, it can be denoted as a $4^6 6^8$ structure. That cage is large enough to storage H_2, H_2O, CO_2, or other small molecules inside. Here we have undertaken the study of the adsorption of H_2O and H_2 inside and outside of $(Ta@Si_{16}F)_6$ aggregates and wires. This study is motivated by the search of new solid materials for hydrogen storage in mobile or stationary devices, the latter with (hopefully) near-term applications. The literature on this subject is extensive, references [93, 94] are only some examples.

As a first step we study the adsorption of atomic and molecular hydrogen (H and H_2) on the $Ta@Si_{16}F$ unit in order to characterize the different adsorption sites. The main results of our calculations are the following: The adsorption energy of H_2O inside the $(Ta@Si_{16}F)_6$ aggregate, (Figure 8.6 (a)), is 0.255 eV, and 0.287 eV for the $(Ta@Si_{16}F)_6$ nanowire. A single H_2 molecule is captured in

the center of the aggregate (Figure 8.6 (a)) with adsorption energy 0.015 eV, bond length 0.790 Å, and zero magnetic moment. On the other hand, the adsorption energy of H_2 inside of the periodic $(Ta@Si_{16}F)_6$ nanowire is 0.025 eV. Finally, the adsorption energy per H_2 molecule when n H_2 molecules are adsorbed outside of the $(Ta@Si_{16}F)_6$ aggregate is 0.060 eV for $n = 1$ and 0.054 eV for $n = 6$, see Figure 8.9.
In this chapter we will explain and discuss these results in detail.

8.1 Adsorption of H and H_2 on $Ta@Si_{16}F$ unit

In this section we investigate the favorable sites and configurations for adsorption of atomic and molecular hydrogen on a single super-atom unit. The adsorption energy of A (=H, H_2) is defined as

$$E_{ads}(A\text{-Ta@Si}_{16}\text{F}) = E(\text{Ta@Si}_{16}\text{F}) + E(A) - E(A\text{-Ta@Si}_{16}\text{F}).$$

8.1.1 Atomic hydrogen chemisorption on $Ta@Si_{16}F$ unit

A single H atom prefers to bind on top of a Si atom of $Ta@Si_{16}F$ instead of bridge or hollow sites, as shown in Figure 8.1. The binding energy, HOMO-LUMO gap, electric dipole, distances Ta-Si and Si-H are given in Table 8.1 for the several on-top sites. The binding energy ranges between a maximum of 1.98 eV on top of a Si^2 in the equatorial plane and 1.82 eV for those Si^1 atoms closer to the F atom. Thus, H atoms become chemically bonded on top of Si atoms with a typical distance Si-H $\sim$ 1.53 Å. On the other hand the angle Ta-Si-H ranges from $\sim 154° - 178°$, i.e. the H atom deviates from the line Ta-Si $\sim 8° - 26°$. The Ta-Si average distance is 2.93 Å, that is the chemisorption of a single H atom maintains the original size of the unit.

The largest HOMO-LUMO gap (1.25 eV) occurs for H chemisorbed on the Si^1 atoms in the opposite side to the F atom ($Si_{[15]}$ and $Si_{[16]}$), and the smaller for H on the Si^2 atoms closer to F and its mirrors (about 0.60 eV). The larger dipole moments occurs for the H atom on a Si^2 atom on the opposite side to the Fluorine, that is, on atom $Si^2_{[9]}$, and for H on the Si^1 atoms nearby to F. The smallest dipole moment occurs for H atom “on top” of the Si^2 nearest to F ($Si^2_{[5]}$), which is opposite to $Si^2_{[9]}$. This is also the most stable one, with the largest deviation of H from the Ta-Si line.

Contrary to intuition, the H atom does not chemically bind to the F atom. The HF molecule in gas phase has a binding energy $\sim$ 5.88 eV, bond distance 0.917 Å, and dipole moment 1.86 Debye. Instead the adsorption of H on the F atom of Ta@Si_{16}F to form Ta@Si_{16}F-H has a binding energy $\sim$ 0.015 eV, 2.90 Å for the HF distance, and only the dipole moment of the compound, 1.82 Debye, is similar to the experimental one of the H-F molecule in gas phase. Thus, the H atom is physisorbed on top of the F atom. The result that, in the Ta@Si_{16}F-H, the Si-F bond is stronger than that of the H-F bond, can be explained as follows: The experimental bond enthalpy of a SiF_4 molecule is about 2388 kJ/mol, then one can estimate the average bond strength of a single Si-F bond as $\sim$ 597 kJ/mol, to be compared with the experimental bond enthalpy of H-F, which is $\sim$ 568 kJ/mol. This stronger bond Si-F compared to that of H-F has been realized in X-ray photospectroscopy on HF passivated silicon surfaces [95, 96]. We see that the Si prefers to be passivated by the F atom, and an additional H atom becomes only slightly physisorbed on that F atom.

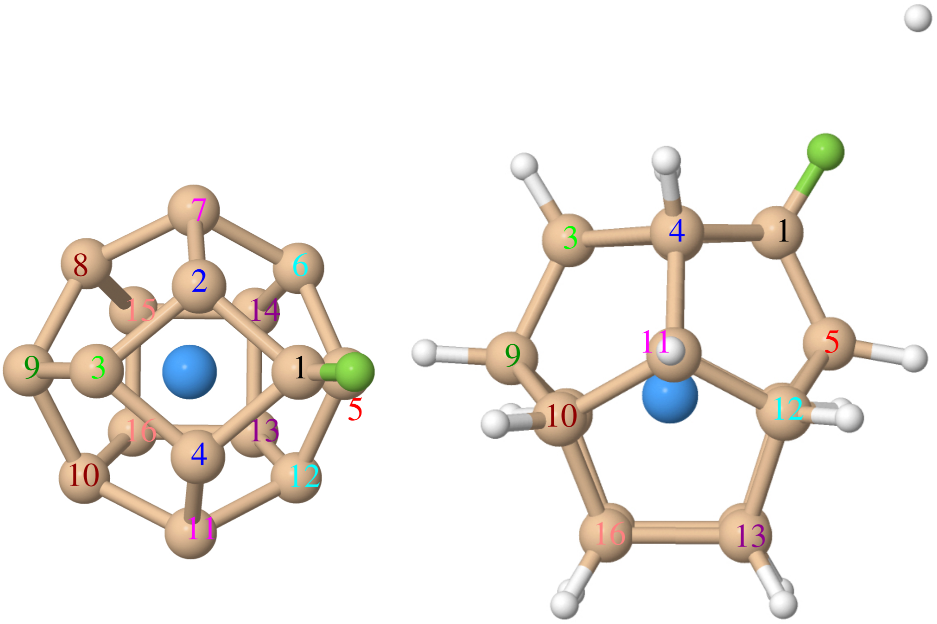

Figure 8.1: Left: Equivalent sites of Ta@Si_{16}F are numbered with the same color. Right: Adsorption geometries of atomic hydrogen on the several sites of Ta@Si_{16}F which are referred to in Table 8.1.

Table 8.1: Adsorption energy (per H atom) (eV), HOMO-LUMO gap (eV), electric dipole (Debye), average Ta-Si distance (d^{avg}_{Ta-Si}) (Å), Si(F)-H distance $d_{Si(F)-H}$ (Å), angle Ta-Si(F)-H ($\angle$(Ta-Si-H)), and the deviation angle from the Ta-Si line ($\angle_{deviation}$) for an H atom on top of a $Si_{[site]}$ (for the *site* numbers see Figure 8.1) and on F. When two sites are given they are the "mirror" one of the other.

H on top of	E_{ads}	*gap*	Dipole	d^{avg}_{Ta-Si}	d_{Si-H}	$\angle$(Ta-Si-H)	$\angle_{deviation}$
$Si_{[5]}$	1.98	0.65	1.40	2.93	1.53	153.70°	26.30°
$Si_{[8,10]}$	1.97	0.72	1.69	2.93	1.53	173.33°	6.67°
$Si_{[13,14]}$	1.95	1.24	1.77	2.94	1.54	174.33°	5.67°
$Si_{[15,16]}$	1.93	1.25	1.70	2.94	1.54	173.06°	6.94°
$Si_{[9]}$	1.90	0.54	2.55	2.94	1.53	171.53°	8.47°
$Si_{[6,12]}$	1.87	0.78	1.92	2.93	1.53	174.79°	5.21°
$Si_{[7,11]}$	1.87	0.70	1.99	2.93	1.53	169.27°	10.73°
$Si_{[3]}$	1.82	1.11	1.81	2.94	1.54	177.58°	2.42°
$Si_{[2,4]}$	1.82	1.15	2.30	2.94	1.54	170.35°	9.66°
F	0.02	1.44	1.82	2.93	2.90	177.81°	2.19°

8.1.2 Molecular H_2 physisorption on Ta@Si_{16}F unit

The H_2 molecule in gas phase is a very stable system which barely interacts with its surroundings. A single H_2 molecule becomes physisorbed preferably on bridge (Si-Si) position of the Ta@Si_{16}F unit with phsyisorption energies between 0.029 eV and 0.042 eV, and average distance H_2-(Si-Si) $\sim$ 3.69 Å. The Ta-Si average distance, 2.93 Å, is not modified after physisorption of a H_2 molecule, and the dipole moment for each configurations remains similar to that of the free Ta@Si_{16}F unit.

In most cases the H_2 molecule orients in the direction of the line joining the Ta with the $(\text{Si-Si})_{edge}$. Another way to say this is that, if one thinks of the Ta@Si_{16}F unit as a sphere with the Ta as its center, the H_2 molecules orient radially in the direction of the *edge* with a characteristic distance, measured from the center-H_2 to center distance of the edge, of 3.69 Å.

The few H_2 molecules that depart from that behavior are those nearest to the F atom (on edges 1, 4, and 5, see Figures 8.2 and 8.3 left and middle). In those cases the H_2 molecule are tilted in the direction of the F and its center a little bit shifted, with larger distance than the average. An illustration of the physisorption geometries is provided in Figure 8.2. In Table 8.2 are given the energy, distance, HOMO-LUMO gap, and dipole for the different physisorption sites. From Table 8.2 we see that the more favorable sites are those edges closer to the F atom (Figure 8.2 (a) and (b)), and at the same time they are more apart from the Silicon edges than the others, with an average distance H_2-(Si-Si) $\sim$ 3.90 Å.

As we have seen, a H_2 molecule prefers to be on bridge position and radially oriented. Thus, we use this recipe to construct the compound (Ta@Si_{16}F)-$(H_2)_{24}$, made by the simultaneous physisorption of 24 H_2. The geometry adopted by such a complex is that of the **truncated** D_{4d} unit (Ta@Si_{16}F without the F atom), but we have found that this geometry is not preserved after relaxation. The final positions of the 24 H_2 are the vertexes of a **distortion of the truncated** D_{4d} polyhedron, with an average adsorption energy per H_2 molecule of 0.041 eV.

Thus, physisorption of successive H_2 molecules proceeds independently.

In order to estimate how much the adsorption energy increases using a density functional which incorporates the long range correlation effects, we have calculated the physisorption energies on edges **1 and 10** (lower and higher energy states) using the recent self-consistent van der Waals density functional implementation of Soler et al [65]. We obtained increases about 20% and 28%, respectively, in the physisorption energy. These results for the increase of the H_2 adsorption energy are similar to those of the H_2O on hydrogen-passivated Si nanowires calculated recently by Hmiel and Xue [97]. These authors obtained $0.043 - 0.077$ eV (depending on the crystallographic surface) physisorption energy of H_2O using the GGA-PBE density functional and a correction of $0.02 - 0.03$ eV using an empirical van der Waals correction of Grimme [98]. The distance $H_2 - edge$ is larger for the van der Waals calculation than for the GGA-PBE one. The H-H distance doesn't changes appreciably with respect to that of the free H_2 molecule.

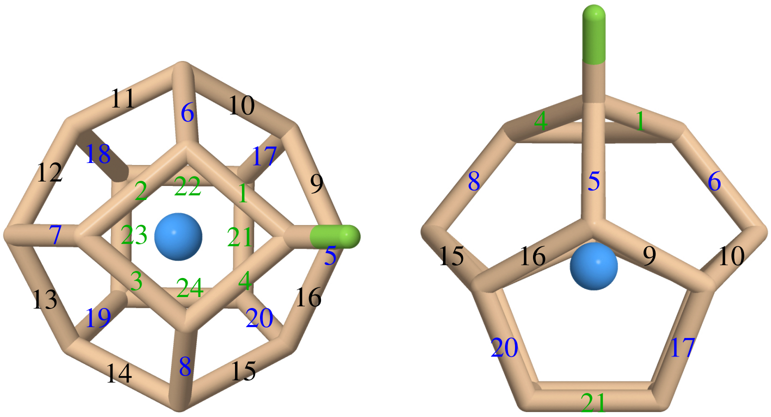

Figure 8.2: Left and Right: Different edges-sites to physisorb a H_2 molecule. In green: Si^1-Si^1 edges, In black: Si^2-Si^2edges, In blue: Si^1-Si^2 edges.

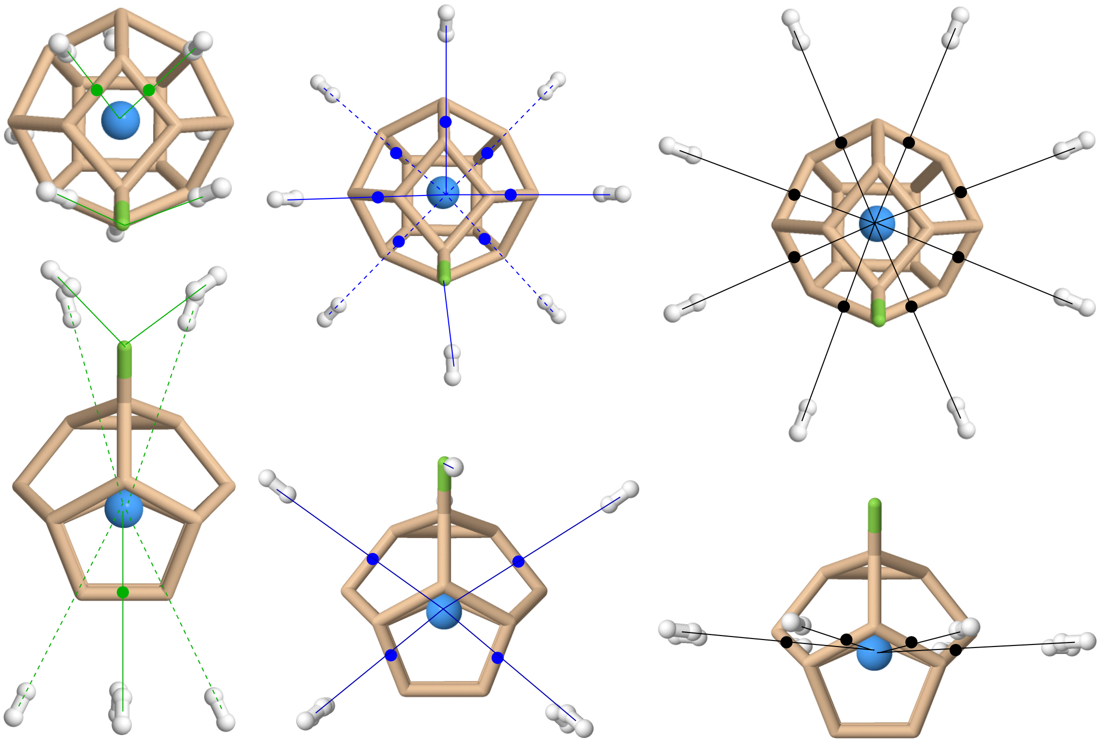

Figure 8.3: Different edge-sites to physisorb a H_2 molecule. From left to right: H_2 on top of a: Si^1-Si^1 edge, Si^1-Si^2 edge, Si^2-Si^2edge.

Table 8.2: Adsorption energy (per H_2 in eV), HOMO-LUMO gap (eV), dipole (Debye), average Ta-Si (Å) distance (d^{avg}_{Ta-Si} in Å), *edge*-H_2 distance (d_{edge-H_2}), for an H_2 molecule on top of a (Si-Si)$_{[edge]}$ (for the *edge* numbers see Figure 8.2). When two edges are given they are the "mirror" one of the other.

Edge Number	E_{ads}	*gap*	Dipole	d^{avg}_{Ta-Si}	d_{edge-H_2}
(Si-Si)$_{[1,4]}$	0.042	1.44	1.81	2.93	3.90
(Si-Si)$_{[5]}$	0.039	1.44	1.86	2.93	3.88
(Si-Si)$_{[6,8]}$	0.037	1.44	1.76	2.93	3.62
(Si-Si)$_{[17,20]}$	0.036	1.43	1.55	2.93	3.72
(Si-Si)$_{[18,19]}$	0.036	1.44	1.54	2.93	3.72
(Si-Si)$_{[9,16]}$	0.032	1.44	1.73	2.93	3.69
(Si-Si)$_{[2,3]}$	0.032	1.44	1.72	2.93	3.65
(Si-Si)$_{[7]}$	0.032	1.44	1.71	2.93	3.59
(Si-Si)$_{[11,14]}$	0.031	1.44	1.67	2.93	3.65
(Si-Si)$_{[23]}$	0.031	1.43	1.51	2.93	3.70
(Si-Si)$_{[12,13]}$	0.031	1.43	1.60	2.93	3.66
(Si-Si)$_{[22,24]}$	0.030	1.44	1.54	2.93	3.69
(Si-Si)$_{[21]}$	0.030	1.43	1.59	2.93	3.65
(Si-Si)$_{[10,15]}$	0.030	1.44	1.72	2.93	3.64
24·H_2 on (Si-Si)	0.041	1.43	1.72	2.92	3.83

8.2 Adsorption: H, H_2 and H_2O inside $(\text{Ta@Si}_{16}\text{F})_6$

We define the adsorption energy as

$$E_{ads}[(nY@X)] = E[X] + nE[Y] - E[nY@X],$$

where $X = (\text{Ta@Si}_{16}\text{F})_6^{cluster}$, $(\text{Ta@Si}_{16}\text{F})_6^{wire}$, and n is the number of Y (= H, H_2, H_2O) molecules.

In the next sections we present the results for the adsorption of H, H_2, and H_2O inside the $(\text{Ta@Si}_{16}\text{F})_6$ cluster and wire.

8.2.1 Adsorption: n H inside $(\text{Ta@Si}_{16}\text{F})_6$ $n = 1, 2$

Adsorption: One H inside $(\text{Ta@Si}_{16}\text{F})_6$

A single H inside the barrel (shown in Figure 7.2) binds mainly in four configurations: (i) "on top" of one Si, (ii) in "hollow position" , between two Silicons of *different* $\text{Ta@Si}_{16}\text{F}$ units, (iii) in "bridge position" position, between two Silicons of *the same* $\text{Ta@Si}_{16}\text{F}$ unit, and (iv) in a "broken bond position", breaking a Si^1-Si^1 bond to create a Si^1-H-Si^1 one. The more stable configuration is "on top" of a Si^1 (Figure 8.4 (a)), heavily distorting the geometry of the system, with binding energy 1.46 eV. The second more stable configuration has only 0.010 eV higher energy. In this case the chemisorbed H atom does not distort the local geometry. This chemisorption is of hollow type. (Figure 8.4 (b)), with the H in the middle of a hexagon, connecting two Si^1 belonging to different $\text{Ta@Si}_{16}\text{F}$ units. Another chemisorption configuration has the H in bridge position connecting two Si^1 atoms of the same $\text{Ta@Si}_{16}\text{F}$ unit (Figure 8.4 (c)), this about 0.20 eV higher energy than the hollow configuration. Finally we have found another "broken bond" configuration, which tends to break the Si^1-Si^1 bond, leading to a nearly linear Si^1-H-Si^1 edge (Figure 8.4 (d), (e), and (f)).

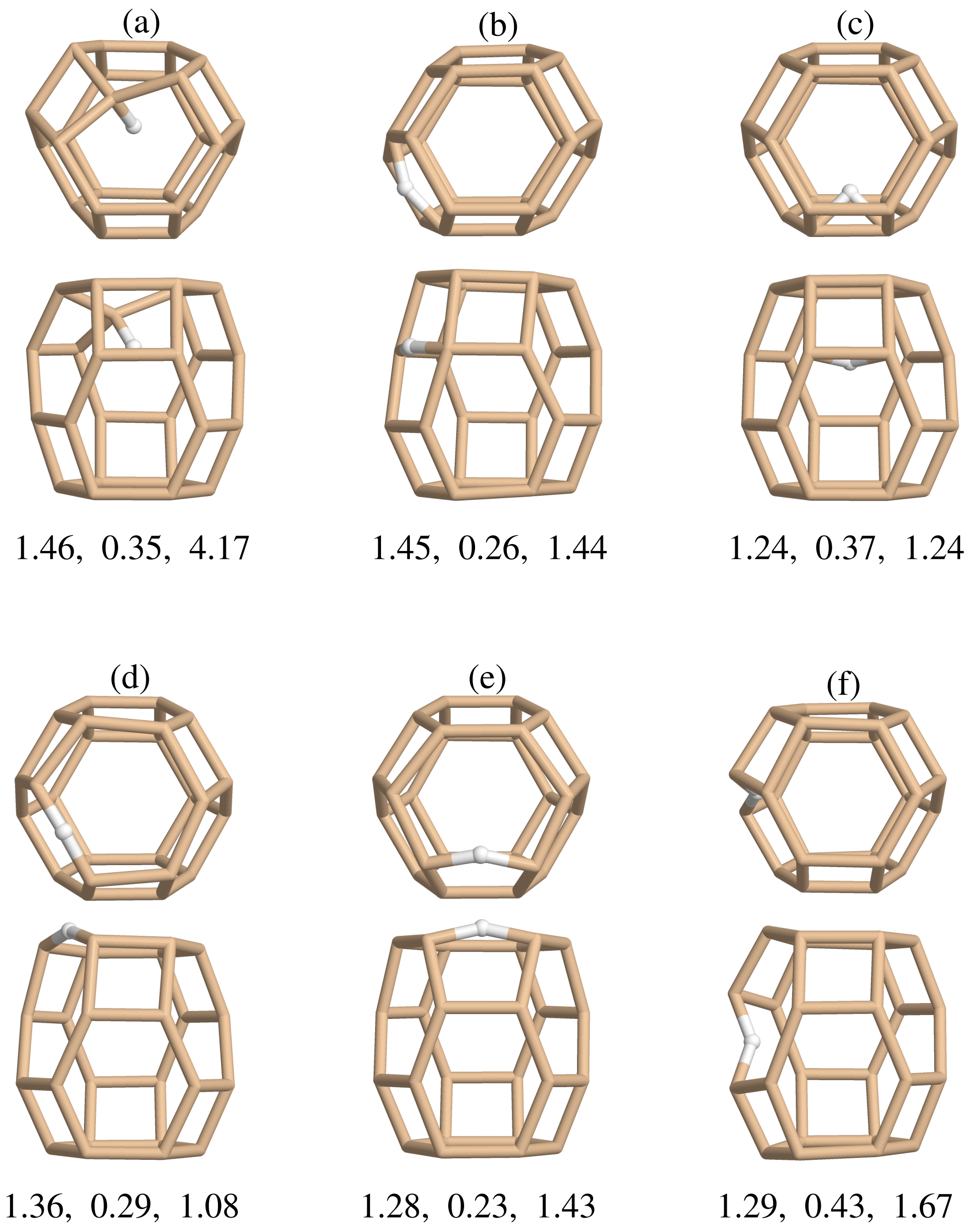

Figure 8.4: "Top" and "side" view of the $H@(TaSi_{16}F)_6$ cluster (only the barrel-shaped structures shown to aid the view). Configurations (a), (b), and (c) are "on top", "hollow", and "bridge" type, respectively. Configurations (d), (e), and (f) are "breaking bond" type. The numbers correspond to adsorption energy (eV), HOMO-LUMO gap (eV), and dipole (Debye).

Adsorption: Two H atoms inside $(\mathbf{Ta@Si_{16}F})_6$

When adding a second H atom to the previous configurations, the inner structure geometry is distorted, except for the bridge-like type ones. In Figure 8.5 are shown the more stable equilibrium geometries. Configuration (a) is the most stable one, with a binding energy of 3.45 eV; in this case both H are “on top” position. Configurations (b) and (c) are degenerate, with a binding energy of 3.25 eV. Case (b) has both H in “hollow” position (compare with 8.4 (b)), while case (c) “on top” position. Configurations (d)–(f), have ~ 0.70 eV smaller chemisorption energy with with both H atoms in “broken bond” position, one of them in the same position 8.4 (e). These configurations tends to close the HOMO-LUMO gap. Configurations (d) and (e) have the additional H in quasi-equivalent positions as 8.4 (d). Finally, configuration (f) has both H in positions like 8.4 (e).

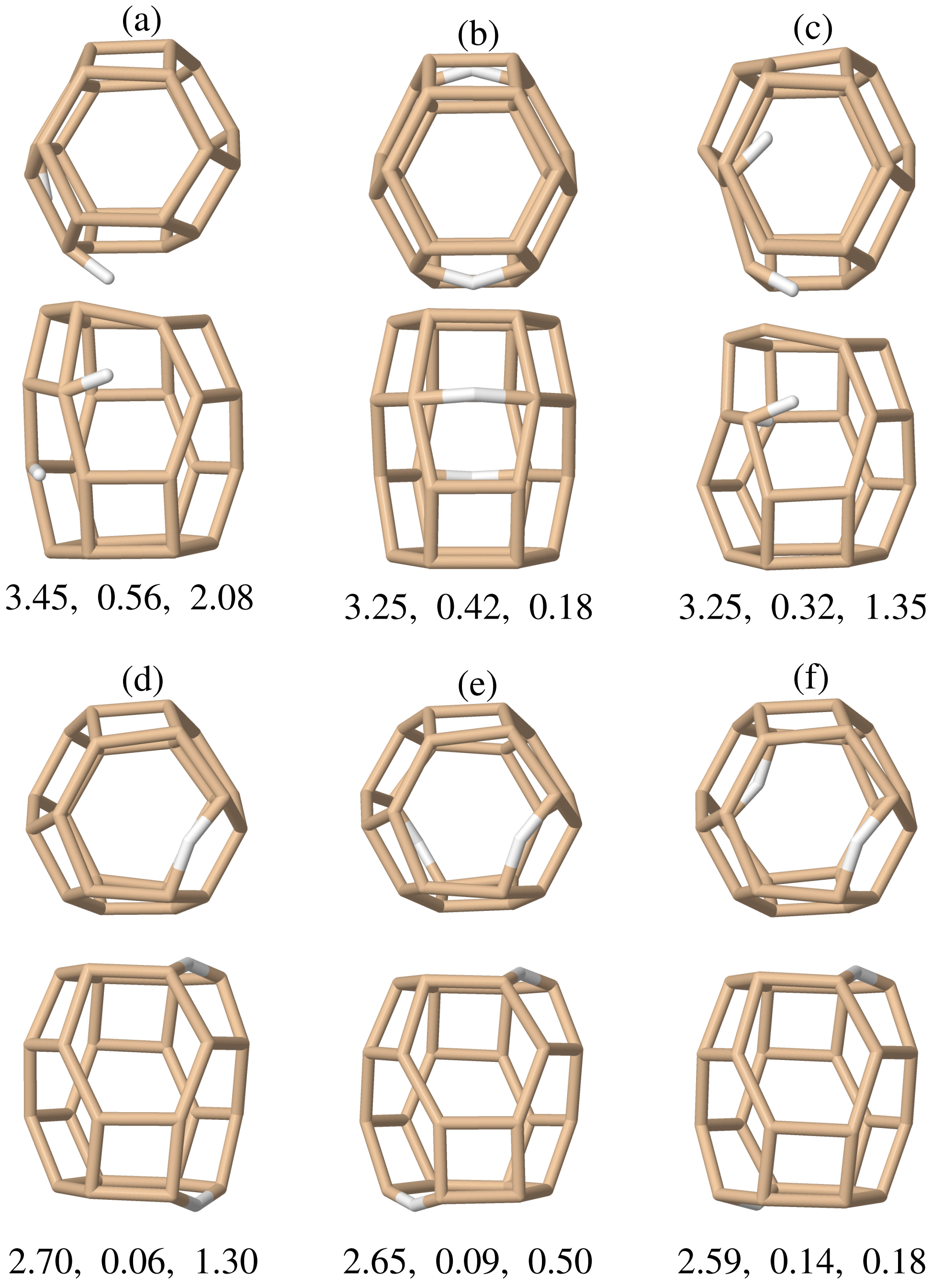

Figure 8.5: "Top" and "side" view of the $2H@(TaSi_{16}F)_6$ more stable configurations (only the barrel-shaped structures shown to aid the view). The numbers correspond to adsorption energy (eV), HOMO-LUMO gap (eV), and dipole (Debye).

8.2.2 Adsorption: $n{\cdot}\mathrm{H}_2$ inside $(\mathrm{Ta@Si}_{16}\mathrm{F})_6$ $(n = 1 - 3)$

Figure 8.6, shows the structures for one H_2 molecule inside the inner barrel shaped structure of the $(Ta@Si_{16}F)_6$ cluster and wire. The H_2 molecule prefers to be in the plane perpendicular to the cluster/wire axis at the center of the inner barrel, as shown in Figure 8.6 (a) and (b). Configuration (b) corresponds to a rotation of (a) around the cluster/wire axis. It leaves the HOMO-LUMO gap unchanged, but increases the total energy by a tiny amount. Such difference in the relative orientations leads to a small change in the dipole of ~ 0.030 Debye. Finally, configuration (c) corresponding to the H_2 molecule oriented along the cluster/wire axis, is not bound (the binding energy is negative).

The binding energy of one H_2 inside the wire increases as compared to the cluster, in a range between $60 - 90\%$.

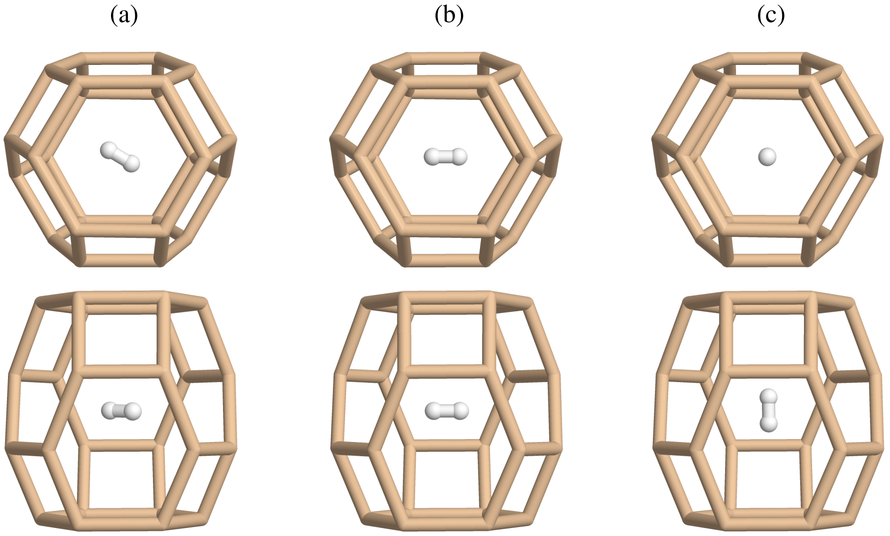

[C]: 0.015, 0.434, 0.089
[W]:0.024, 0.434, 0.089

[C]: 0.013, 0.435, 0.120
[W]: 0.025, 0.435, 0.128

[C]: –0.008, 0.430, 0.052
[W]: –0.014, 0.430, 0.052

Figure 8.6: "Top" and "side" view of the $H_2@(TaSi_{16}F)_6$ clusters and wires (only the barrel-shaped structures shown to aid the view). The numbers correspond to adsorption energy (eV), HOMO-LUMO gap (eV), and dipole (Debye). [C] stands for Cluster, [W] for Wire. **Lower energy states in bold**.

We have found that there are no bound structures of $n{\cdot}H_2$ molecules adsorbed inside the barrel shaped structures for $n > 1$, that is the adsorption energy, as defined above, is negative. Figure 8.7 shows such structures for the cluster and wire. Configurations (a) and (b) contains the 2 H_2 in parallel planes, one above and one below the equatorial plane, with an H_2-H_2 distance $\sim$ 2.40 Å. In case (a) the H_2 axes are perpendicular to each other, while in case (b) they are parallel. Case (b) was also studied in the wire. In this case the binding energy is less negative than for the cluster (that is, it cost less energy to hold together the two H_2 in the cavity) and the HOMO-LUMO gap and the dipole moment drastically decrease with respect to the aggregate case.

Configurations (c) and (d) in Figure 8.7, correspond to 3 H_2 molecules inside the cluster and wire. Configuration (c) for the cluster has 2 H_2 inside the barrel and one H_2 physisorbed H_2 outside the cavity; in the case of the wire system the outer H_2 lies between two $(Ta@Si_{16}F)_6$ units. The binding energy of that H_2 in the wire is 0.04 eV, that is, about a factor two larger than the configuration of H_2 inside de cavity 8.6 (b).

The 3 H_2 in configuration (d) form a triangle with sides (2.73, 2.04, 2.19) Å in a plane which contains the axis of the cluster/wire. In this configuration we need $\sim$ 1.06 eV (0.97 eV) to put 3 H_2 inside the cluster (wire).

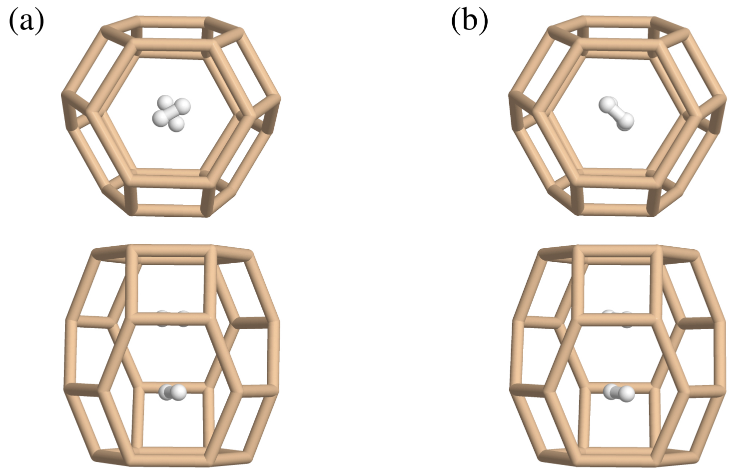

[C]: −0.26, 0.45, 0.19

[C]: −0.26, 0.45, 0.16
[W]: −0.18, 0.18, 0.05

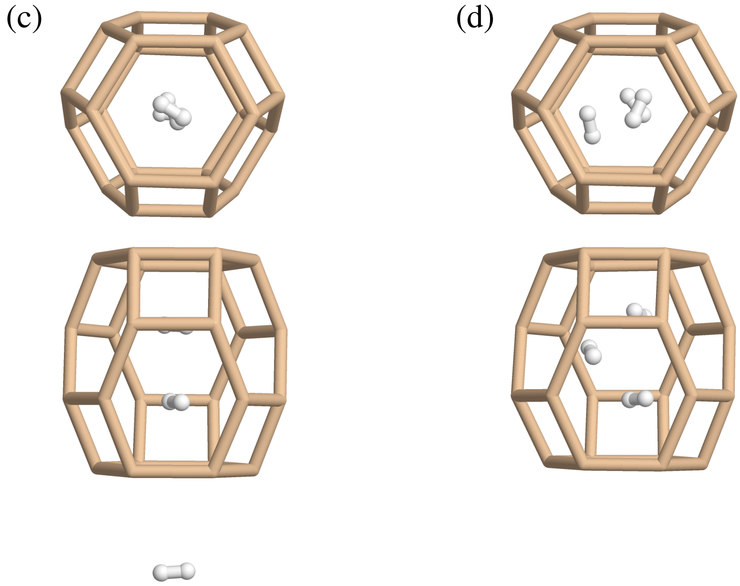

[C]: −0.21, 0.46, 0.13
[W]: −0.28, 0.13, 0.06

[C]: −1.06, 0.46, 0.31
[W]: −0.97, 0.15, 0.07

Figure 8.7: “Top” and “side” view of the $2H_2@(TaSi_{16}F)_6$ and $3H_2@(TaSi_{16}F)_6$ clusters (only the barrel-shaped structures shown to aid the view). The numbers correspond to adsorption energy (eV), HOMO-LUMO gap (eV), and dipole (Debye). [C] stands for Cluster, [W] for Wire.

8.2.3 Adsorption: H_2O inside $(Ta@Si_{16}F)_6$

Our results show that the encapsulation of a H_2O molecule into the $(Ta@Si_{16}F)_6$ is also possible. The encapsulation leaves the $(Ta@Si_{16}F)_6$ structure unaltered, but deforms a little bit the encapsulated water molecule. The distance O-H after encapsulation increases a little bit, 0.98 Å in the free molecule compared to 0.99 Å while encapsulated. The angle H-O-H, on the other hand, decreases after encapsulation. A summary of this is found in Table 8.3. Encapsulated structures have the O atom at the center of the barrel-shaped-inner structure of the $(Ta@Si_{16}F)_6$, with slightly different relative orientations of the H atoms. The lowest energy state has a binding energy of 0.255 eV, and is shown in Figure 8.8 (a). In this phase both H atoms are "above" the plane in the center of the barrel, each H pointing in the direction of a Si^1 from different $Ta@Si_{16}F$ units (in the figure they are marked with a blue dot). Interestingly, the adsorption of H_2O inside the $(Ta@Si_{16}F)_6$ wire adopt the same position than in the aggregate, but the adsorption energy increases to 0.287 eV, the HOMO-LUMO gap decreases, and the dipole moment of the system becomes near zero, as it should be.

Structures 8.8 (b) and (c) are practically degenerated. They are rotated $\sim 30°$ around the wire axis with respect to the lowest energy state. In this case the H atoms are also not in the plane, but as opposed to (a), one H goes "above" and one "below" the central plane of the barrel. This "tilting" is more appreciable in (c) than in (b) (where the H_2O molecule practically lies in the plane). Nevertheless their energy are essentially the same, with a difference ~ 0.001 eV.

Table 8.3: Angles H-O-H ($\angle_{H-O-H}$) and distances O-H (d_{O-H}) for the free and encapsulated H_2O in the different configurations, given in Figure 8.8.

	Free H_2O	Encapsulated H_2O		
configuration	Free	(a)	(b)	(c)
d_{O-H}	0.98 Å	0.99 Å	0.99 Å	0.99 Å
$\angle_{H-O-H}$	104.0°	103.8°	103.8°	102.7°

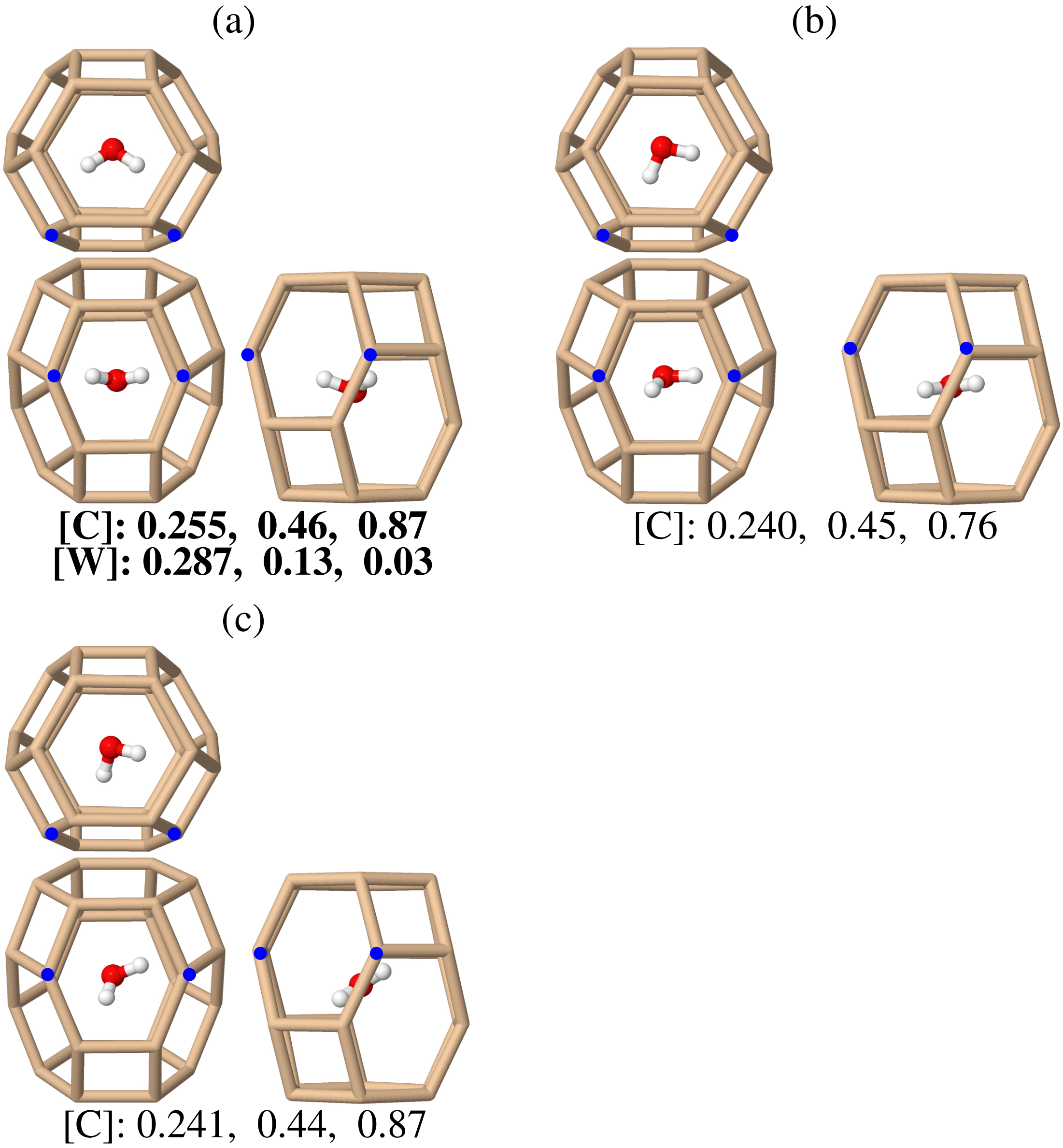

Figure 8.8: Different viewpoints of the $H_2O@(TaSi_{16}F)_6$ clusters and wires (only the barrel-shaped structures shown to aid the view). The numbers correspond to adsorption energy (eV), HOMO-LUMO gap (eV), and dipole (Debye). [C] stands for Cluster, [W] for Wire. Blue dots are only to take track of the viewpoint. **Most stable structure in bold**.

8.3 Adsorption: nH$_2$ (Ta@Si$_{16}$F)$_6$ $n = 1 - 6$

I have also studied studied the adsorption of several H_2 molecules outside the (Ta@Si$_{16}$F)$_6$ aggregate. Figure 8.9 b shows the different more favorable positions of the nH$_2$ molecules for $n = 1 - 6$ physisorbed on the (Ta@Si$_{16}$F)$_6$ cluster.

In Figure 8.9 the H_2 molecule in the black (red) circle is in the middle of the $\mathrm{Si}^2_{[11]}$ ($\mathrm{Si}^2_{[7]}$), $\mathrm{Si}^2_{[5]}$, and $\mathrm{Si}^2_{[9]}$ atoms (see Figure 8.1), at a distance of 3.69 Å, 3.92 Å, and 3.90 Å, respectively. Thus, the relative position of each H_2 molecule with respect to its three nearest Ta@Si$_{16}$F neighbors is the same in all cases, and the contribution to the total energy of consecutively adding a H_2 molecule is nearly independent of the position taken by it. In Table 8.4 the adsorption energy, HOMO-LUMO gap, and dipole are presented for the structures $n{\cdot}$H$_2$ in the range $n = 1, \ldots, 6$; the labels a, b, … represent different moieties for a fixed n. Similar information is given in Figure 8.10. In this figure are also shown several arrangements for each fixed number of molecules. These arrangements differ mainly in the dipole moment.

Compared to the case of H_2 inside the cavity, the physisorption energy is a factor four larger. However, the HOMO-LUMO gap and dipole moment values are similar.

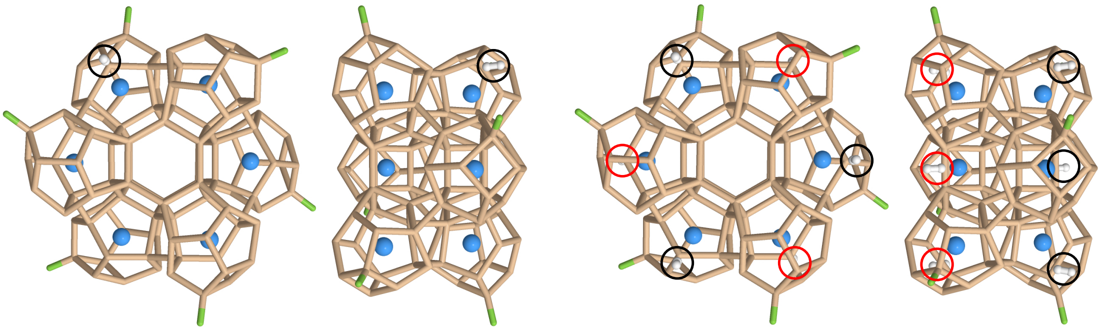

H_2: 0.060, 0.443, 0.104

6H_2: 0.054, 0.445, 0.039

Figure 8.9: "Top" and "side" view of the H_2 on (Ta@Si$_{16}$F)$_6$ and 6H_2 on (Ta@Si$_{16}$F)$_6$ clusters. The numbers correspond to adsorption energy (eV), HOMO-LUMO gap (eV), and dipole (Debye). Black and red circles show the positions of the H_2 molecules.

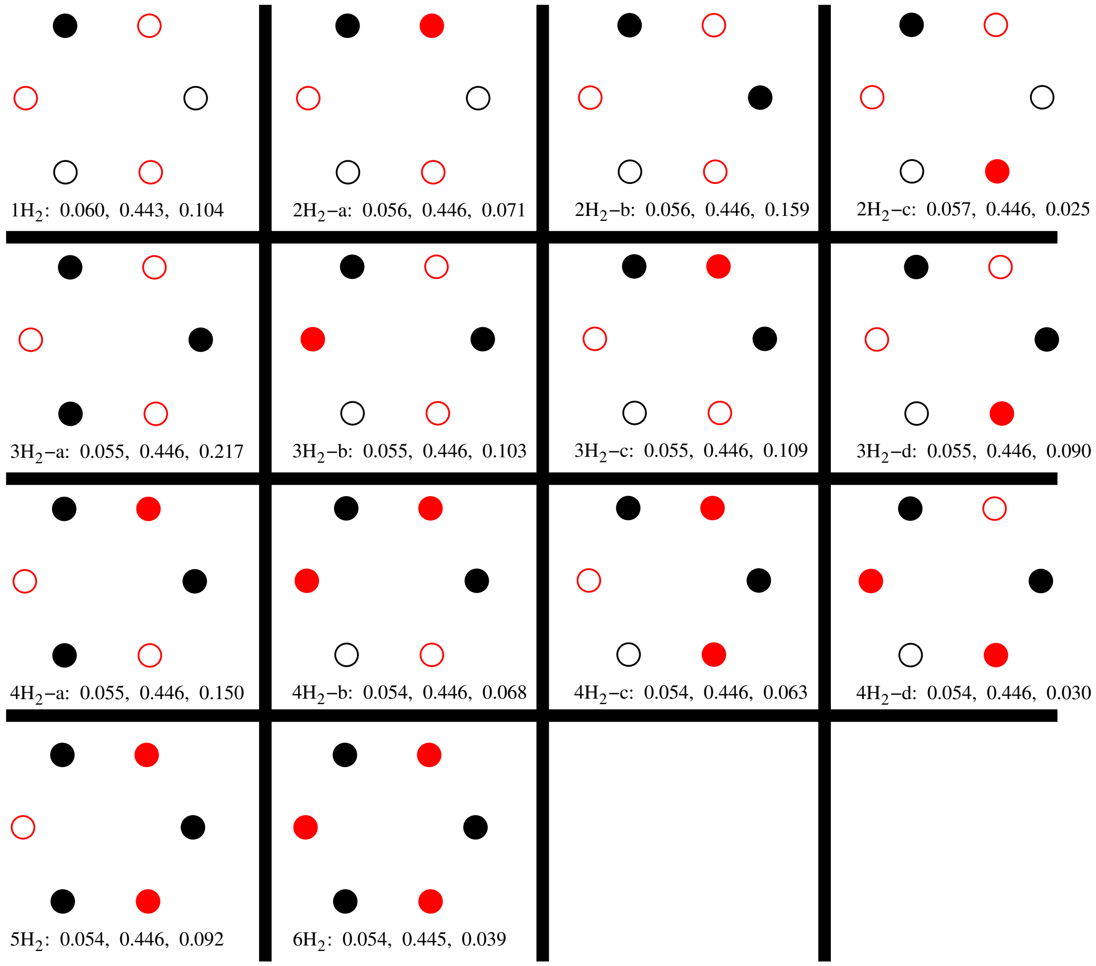

Figure 8.10: Schematic of the positions of $n{\cdot}H_2$ adsorbed outside the $(Ta@Si_{16}F)_6$ structure. The numbers correspond to adsorption energy (per H_2 in eV), HOMO-LUMO gap (eV), and dipole (Debye). Filled black and red circles represent a H_2 molecule in the positions of Figure 8.9.

Table 8.4: Adsorption energy per H_2 (E_{ads} in eV), HOMO-LUMO gap (Δ_{gap} in eV), and dipole (Debye) for the structures $n{\cdot}H_2$ ($n = 1 - 6$). Labels a,b, …are used to differenciate among moieties with a fixed n.

Label	E_{ads}	Δ_{gap}	Dipole
$1{\cdot}H_2$	0.060	0.443	0.104
$2{\cdot}H_2$-a	0.056	0.446	0.071
$2{\cdot}H_2$-b	0.056	0.446	0.159
$2{\cdot}H_2$-c	0.057	0.446	0.025
$3{\cdot}H_2$-a	0.055	0.446	0.217
$3{\cdot}H_2$-b	0.055	0.446	0.103
$3{\cdot}H_2$-c	0.055	0.446	0.109
$3{\cdot}H_2$-d	0.055	0.446	0.090
$4{\cdot}H_2$-a	0.055	0.446	0.150
$4{\cdot}H_2$-b	0.054	0.446	0.068
$4{\cdot}H_2$-c	0.054	0.446	0.063
$4{\cdot}H_2$-d	0.054	0.446	0.030
$5{\cdot}H_2$	0.054	0.446	0.092
$6{\cdot}H_2$	0.054	0.445	0.039

9

Summary

In this thesis we have investigated and characterized the structural and electronic properties of the following systems:

(*i*) $Ta^+@Si_{14-18}$ clusters, (*ii*) $(Ta@Si_{16}F)_{m=1-8}$ aggregates formed by $Ta@Si_{16}F$ molecules, (*iii*) infinite wires formed by stacking triangular $(Ta@Si_{16}F)_3$ twisted 60° each other along the vertical, (*iv*) the cubic phases of bulk $Ta@Si_{16}F$; (*v*) adsorption of H, H_2, and H_2O in the infinite wire described in (*iii*).
All calculations were performed within the density functional theory by means of the SIESTA code using the generalized gradient approximation as parametrized by Perdew-Burke-Ernzernhof for the exchange and correlation potential.

We have found that $Ta^+@Si_m$ clusters shows a peak at $m = 16$ in the binding energy, second energy difference, and HOMO-LUMO gap, with two structures in different symmetries separated by only 0.04 eV in the *binding energy.* The most stable $Ta^+@Si_m$ cation is a distorted Frank-Kasper polyhedron with C_{3v} symmetry; the second most stable is a fullerene-like structure with D_{4d} symmetry. However, the molecule $Ta@Si_{16}F$ with D_{4d} symmetry is 0.04 eV more stable than that with C_{3v} symmetry. We have optimized several $(Ta@Si_{16}F)_{m=1-8}$ aggregates which contain the $Ta@Si_{16}F$ unit with D_{4d} symmetry; among these aggregates, $(Ta@Si_{16}F)_6$, is an interesting case, the most stable one formed by vertically stacking two triangular $(Ta@Si_{16}F)_3$ aggregates rotated by a 60° angle. The infinite wire formed with that $(Ta@Si_{16}F)_6$ aggregate as unit cell has 1.87 eV of cohesive energy. Furthermore we study the adsorption of H_2, and H_2O towards this infinite wire.

We have optimized also a metastable fcc bulk phase. From a Birch-Murnaghan fit to that phase it results a cohesive energy of 0.84 eV at a lattice constant of 12.27 Å, with bulk modulus 7.55 GPa, a phase stability to isotropic compression smaller than 0.75 GPa, and a band gap of 0.20 eV. Using the values of hardness of Ta@$Si_{16}F$ molecules, we estimated a correction factor ~ 3 to that small band gap. For that meta-stable solid we performed a 13.5 ps run of first principles molecular dynamics annealing at 300 K and constant volume, and we found that the Ta@$Si_{16}F$ supermolecule in the fcc cell becomes severely distorted after 5 ps.

Results on the adsorption of small molecules are as follows. (*i*) Atomic chemisorption of H atoms on a single Ta@$Si_{16}F$ unit occurs preferably on top of Si atoms with binding energy ~ 1.90 eV. (*ii*) Molecular physisorption of H_2 on a single Ta@$Si_{16}F$ unit occurs with binding energies in the range $0.030 - 0.040$ eV. Long-range van der Waals effects increase the physisorption energy about $20 - 30\%$. The more favorable physisorption sites are in bridge positions on the Si-Si edges. Simultaneous physisorption of 24 H_2 molecules in those positions leads to a 0.040 eV per H_2 binding energy. (*iii*) Atomic chemisorption of H atoms inside the Ta@$Si_{16}F_6$ aggregate occurs preferably in the sequence: "on top" (~ 1.46 eV), "hollow" (~ 1.45 eV), "bridge" (~ 1.24 eV). Configurations with the H breaking the Si-Si bond are found with binding energies (~ 1.35 eV) lying between the "hollow" and "bridge" configurations. (*iv*) Molecular physisorption of H_2 outside the Ta@$Si_{16}F_6$ is more favorable than inside (0.060 eV vs. 0.015 eV). Only one H_2 can be physisorbed inside that complex, lying in the equatorial plane of the cavity. A position along the cluster/wire axis is not bound. (*v*) A single H_2O molecule is physisorbed in the middle of the inner cavity of the Ta@$Si_{16}F_6$ aggregate (wire) with binding energy 0.255 eV (0.287 eV).

Bibliography

[1] K.-M. Ho et al., Nature **392**, 582 (1998). 1

[2] V. Kumar, Computational Materials Science **36**, 1 (2006). 1, 25

[3] E. C. Honea et al., Nature **366**, 42 (1993). 1

[4] C. C. Arnold and D. M. Neumark, The Journal of Chemical Physics **99**, 3353 (1993).

[5] M. F. Jarrold and E. C. Honea, The Journal of Physical Chemistry **95**, 9181 (1991).

[6] J. Müller et al., Physical Review Letters **85**, 1666 (2000). 1

[7] I. Rata et al., Physical Review Letters **85**, 546 (2000). 1

[8] X. L. Zhu, X. C. Zeng, Y. A. Lei, and B. Pan, The Journal of Chemical Physics **120**, 8985 (2004).

[9] S. Yoo, J. Zhao, J. Wang, and X. C. Zeng, Journal of the American Chemical Society **126**, 13845 (2004).

[10] S. Yoo and X. C. Zeng, Angewandte Chemie International Edition **44**, 1491 (2005).

[11] S. Goedecker, W. Hellmann, and T. Lenosky, Physical Review Letters **95**, 055501 (2005).

[12] J. Bai et al., The Journal of Physical Chemistry A **110**, 908 (2006).

[13] W. Hellmann et al., Physical Review B **75** (2007).

[14] V. Bazterra et al., Physical Review A **69**, 053202 (2004).

[15] O. Oña et al., Physical Review A **73**, 053203 (2006).

[16] H. Kawamura, V. Kumar, and Y. Kawazoe, Physical Review B **70**, 245433 (2004). 1

[17] H. Kawamura, V. Kumar, and Y. Kawazoe, Physical Review B **71**, 075423 (2005). 1

[18] V. Kumar and Y. Kawazoe, Physical Review Letters **87**, 045503 (2001). 1, 2

[19] J. B. Jaeger, T. D. Jaeger, and M. A. Duncan, The Journal of Physical Chemistry A **110**, 9310 (2006). 1

[20] S. Neukermans et al., International Journal of Mass Spectrometry **252**, 145 (2006). 1

[21] S. M. Beck, The Journal of Chemical Physics **87**, 4233 (1987). 1

[22] S. M. Beck, The Journal of Chemical Physics **90**, 6306 (1989). 1

[23] M. Ohara, Chemical Physics Letters **371**, 490 (2003). 1

[24] K. Koyasu, M. Akutsu, M. Mitsui, and A. Nakajima, Journal of the American Chemical Society **127**, 4998 (2005). 1, 30

[25] K. Koyasu, J. Atobe, M. Akutsu, M. Mitsui, and A. Nakajima, The Journal of Physical Chemistry A **111**, 42 (2007). 2, 22, 30, 33

[26] H. P. Cheng, R. Berry, and R. Whetten, Physical Review B **43**, 10647 (1991). 2

[27] K. Jackson, E. Kaxiras, and M. R. Pederson, The Journal of Physical Chemistry **98**, 7805 (1994).

[28] K. Jackson and B. Nellermoe, Chemical Physics Letters **254**, 249 (1996). 2

[29] J. U. Reveles and S. Khanna, Physical Review B **74**, 035435 (2006). 2

[30] A. R. Leach, *Molecular Modelling: Principles and Applications*, Prentice Hall, 2 edition, 2001. 3, 6

[31] P. Söderlind, *Theoretical Studies of Elastic, Thermal, and Structural Properties of Metals*, Reprocentralen HSC, Uppsala, 1994. 3

[32] K. Schwarz and P. Blaha, Computational Materials Science **28**, 259 (2003). 3

[33] R. G. Parr, Annual Review of Physical Chemistry **34**, 631 (1983). 6

[34] E. Wimmer, *Electronic Structure Methods*, NATO ASI Series C498, Dordrecht, Kluwer, 1997. 6

[35] P. Hohenberg and W. Kohn, Physical Review **136**, B864 (1964). 7

[36] W. Kohn and L. Sham, Physical Review **23**, A1133 (1965). 8

[37] D. R. Hartree, The Wave Mechanics of an Atom with a Non-Coulomb Central Field. Part I. Theory and Methods, volume 24, pages 89–110, 1927. 8

[38] J. A. Pople and R. K. Nebert, The Journal of Chemical Physics **22**, 571 (1954). 10

[39] L. Thomas, The calculation of atomic fields, volume 22, pages 542–548, 1927. 10

[40] E. Fermi, Z. Phys. **48**, 73 (1928). 10

[41] P. A. M. Dirac, Note on Exchange Phenomena in the Thomas Atom, volume 26, page 376, 1930. 10

[42] P. Gombas, *Die statistischen Theorie des Atomes und Ihre Andwendungen*, Wein: Springer-Verlag, 1949. 10

[43] N. H. March, **6**, 1 (1957).

[44] N. H. March, *Self-Consistent Fields in Atoms*, Oxford: Pergamon, 1957.

[45] E. H. Lieb, Phys. Rev. Lett. **46**, 457 (1981). 10

[46] D. M. Ceperley and B. J. Alder, Physical Review Letters **45**, 566 (1980). 11

[47] O. Gunnarsson and B. Lundqvist, Physical Review B **13**, 4274 (1976). 12

[48] J. C. Slater, *Quantum Theory of Molecules and Solids Volume 4: The Self-consistent Field for Molecules and Solids*, McGraw-Hill, New York, 1974. 12

[49] J. P. Perdew and A. Zunger, Physical Review B **23**, 5048 (1981). 12, 14

[50] S. H. Vosko, L. Wilk, and M. Nusair, Canadian Journal of Physics **58**, 1200 (1980). 12

[51] D. C. Langreth and J. P. Perdew, Physical Review B **21**, 5469 (1980). 12

[52] J. P. Perdew and Y. Wang, Physical Review B **33**, 8800 (1986). 12

[53] J. P. Perdew, K. A. Jackson, M. R. Pederson, D. J. Singh, and C. Fiolhais, Physical Review B **46**, 6671 (1992). 12

[54] J. P. Perdew, K. Burke, and M. Ernzerhof, Physical Review Letters **77**, 3865 (1996). 12, 13, 18

[55] J. P. Perdew, K. Burke, and Y. Wang, Physical Review B (1996). 13

[56] J. P. Perdew, in *Electronic Structure of Solids 91*, Berlin, 1991, Akademie Verlag. 13

[57] Y. Wang and J. P. Perdew, Physical Review B **43**, 8911 (1991). 13

[58] D. C. Langreth et al., Journal of Physics: Condensed Matter **21**, 084203 (2009). 13

[59] F. Aguilera-Granja, L. C. Balbás, and A. Vega, The Journal of Physical Chemistry A **113**, 13483 (2009). 13

[60] A. Aguado, A. Largo, A. Vega, and L. C. Balbás, Chemical Physics , 10.1016/j.chemphys.2011.07.032 (2011), (to appear). 13

[61] E. M. Fernández and L. C. Balbás, Physical Chemistry Chemical Physics , 10.1039/C1CP22455G (2011), (to appear). 13

[62] M. Dion, H. Rydberg, E. Schröder, D. C. Langreth, and B. I. Lundqvist, Physical Review Letters **92**, 246401 (2004). 14

[63] A. Becke and E. R. Johnson, J. Chem. Phys. **127**, 154108 (2007). 14

[64] Y. Zhang and W. Yang, Physical Review Letters **80**, 890 (1998). 14

[65] G. Román Pérez and J. Soler, Physical Review Letters **103**, 096102 (2009). 14, 63

[66] J. M. Soler et al., Journal of Physics: Condensed Matter **14**, 2745 (2002). P. Ordejón, E. Artacho, and J. M. Soler, Physical Review B **53**, R10441 (1996). 15, 18

[67] G. Román Pérez, *Simulación Mecano-Cuántica en Materiales Complejos y Nanoestructuras*, PhD thesis, Universidad Autónoma de Madrid, 2011. 15

[68] E. Fermi, Nuovo Cimento **11**, 692 (1934). 17

[69] J. Lin, A. Qteish, M. Payne, and V. Heine, Physical Review B **47** (1993). 17

[70] A. Rappe, K. Rabe, E. Kaxiras, and J. Joannopoulos, Physical Review B **41**, 1227 (1990).

[71] D. Vanderbilt, Physical Review B **32**, 8412 (1985).

[72] G. Bachelet, D. Hamann, and M. Schlüter, Physical Review B **26**, 4199 (1982).

[73] G. Kerker, Journal of Physics C: Solid State Physics **13**, L189 (1980).

[74] D. Hamann, M. Schlüter, and C. Chiang, Physical Review Letters **43**, 1494 (1979).

[75] N. Troullier and J. L. Martins, Physical Review B **43**, 1993 (1991). 17, 18

[76] L. Kleinman and D. Bylander, Physical Review Letters **48**, 1425 (1982). 17, 18

[77] L. Sham and W. Kohn, Physical Review **145**, 561 (1966). 18

[78] H. J. Monkhorst and J. D. Pack, Physical Review B **13**, 5188 (1976). 18

[79] E. M. Fernández, M. B. Torres, and L. C. Balbás, International Journal of Quantum Chemistry **99**, 39 (2004). 18

[80] M. Torres, E. Fernández, and L. Balbás, Physical Review B **71**, 155412 (2005). 18

[81] M. Torres, E. Fernández, and L. Balbás, Physical Review B **75**, 205425 (2007). 19, 24, 28

[82] G. López Laurrabaquio, M. B. Torres, E. M. Fernández, and L. C. Balbás, Journal of Mathematical Chemistry **48**, 109 (2009).

[83] M. B. Torres, E. M. Fernández, and L. C. Balbás, The Journal of Physical Chemistry C **115**, 335 (2011). 19

[84] C. Kittel, *Introduction to Solid State Physics*, Wiley, New York, 5 edition, 1986. 21, 22

[85] B. Wang, H.-J. Zhai, X. Huang, and L.-S. Wang, The Journal of Physical Chemistry A **112**, 10962 (2008). 21, 22

[86] F. Birch, J. Geophys. Res. **83**, 1257 (1978). 21, 47

[87] E. N. Koukaras, C. S. Garoufalis, and A. D. Zdetsis, Physical Review B **73**, 235417 (2006). 24

[88] J. Lau et al., Physical Review A **79**, 053201 (2009). 26

[89] C. E. Klots, The Journal of Physical Chemistry **92**, 5864 (1988). 30

[90] A. Cohen, P. Mori-Sánchez, and W. Yang, Physical Review B **77**, 115123 (2008). 34

[91] E. N. Brothers, A. F. Izmaylov, J. O. Normand, V. Barone, and G. E. Scuseria, The Journal of Chemical Physics **129**, 011102 (2008). 35

[92] R. S. Mulliken, The Journal of Chemical Physics **23**, 1833 (1955). 53

[93] S. McWhorter, C. Read, G. Ordaz, and N. Stetson, Current Opinion in Solid State and Materials Science **15**, 29 (2011). 57

[94] P. Jena, The Journal of Physical Chemistry Letters **2**, 206 (2011). 57

[95] J. N. Spencer, G. M. Bondner, and L. H. Rickard, *Chemistry: Structure and Dynamics*, John Wiley Sons. 59

[96] B. R. Weinberger, G. G. Peterson, T. C. Eschrich, and H. A. Krasinski, Journal of Applied Physics **60**, 3232 (1986). 59

[97] A. Hmiel and Y. Xue, Physical Review B **83**, 033304 (2011). 63

[98] S. Grimme, Journal of Computational Chemistry **27**, 1787 (2006). 63